J. Fluid Mech. (2008), *vol.* 612, *pp.* 153–200. © 2008 Cambridge University Press
doi:10.1017/S0022112008000918 Printed in the United Kingdom

Trajectory and flow properties for a rod spinning in a viscous fluid. Part 1. An exact solution

ROBERTO CAMASSA[1], TERRY JO LEITERMAN[2]
AND RICHARD M. MCLAUGHLIN[1]

[1]Department of Mathematics, University of North Carolina, Chapel Hill, NC 27599-3250, USA
[2]Department of Mathematics, St Norbert College, DePere, WI 54115-2099, USA

(Received 11 February 2007 and in revised form 28 December 2007)

An exact mathematical solution for the low-Reynolds-number quasi-steady hydrodynamic motion induced by a rod in the form of a prolate spheroid sweeping a symmetric double cone is developed, and the influence of the ensuing fluid motion upon passive particles is studied. The resulting fluid motion is fully three-dimensional and time varying. The advected particles are observed to admit slow orbits around the rotating rods and a fast epicyclic motion roughly commensurate with the rod rotation rate. The epicycle amplitudes, vertical fluctuations, arclengths and angle travelled per rotation are mapped as functions of their initial coordinates and rod geometry. These trajectories exhibit a rich spatial structure with greatly varying trajectory properties. Laboratory frame asymmetries of these properties are explored using integer time Poincaré sections and far-field asymptotic analysis. This includes finding a small cone angle invariant in the limit of large spherical radius whereas an invariant for arbitrary cone angles is obtained in the limit of large cylindrical radius. The Eulerian and Lagrangian flow properties of the fluid flow are studied and shown to exhibit complex structures in both space and time. In particular, spatial regions of high speed and Lagrangian velocities possessing multiple extrema per rod rotation are observed. We establish the origin of these complexities via an auxiliary flow in a rotating frame, which provides a generator that defines the epicycles. Finally, an additional spin around the major spheroidal axis is included in the exact hydrodynamic solution resulting in enhanced vertical spatial fluctuation as compared to the spinless counterpart. The connection and relevance of these observations with recent developments in nano-scale fluidics is discussed, where similar epicycle behaviour has been observed. The present study is of direct use to nano-scale actuated fluidics.

1. Introduction

The motion of fluids on small spatial scales has long been recognized as central to the understanding of many phenomena in microbiology, including the swimming of microorganisms (Hancock 1953; Taylor 1969), the transport of mucus in ciliated tissue (Fulford & Blake 1986; Sleigh, Blake & Liron 1988; Matsui *et al.* 1998), and even the elastic properties of DNA (Smith, Babcock & Chu 1997; Perkins, Smith & Chu 1999). On small scales, the equations of motion are often taken to be the linear quasi-steady Stokes equations. Though a major simplification with respect to the parent Navier–Stokes system, these equations can still be mathematically challenging because of the boundary conditions that arise typically in these applications, where fluid motion is generated by complicated solid, and sometimes flexible, fluid–structure interactions. In turn, this fluid motion interacts with other bodies and walls, is modified, and ultimately forces the structures which created the motion. These sorts of couplings are especially strong in low-Reynolds-number (small-scale, highly viscous or slowly moving) systems as long-range hydrodynamic interactions play a dominant role compared to their high-Reynolds-number counterparts (Pozrikidis 1997). Fortunately, these long-range penalties are mediated by the linearity of the Stokes equations, and the problems are often amenable to either singularity methods or numerical simulations, with the primary challenge being that of handling complex structure geometries.

Recent advances in nano-scale manipulation (Chu 1991; Fisher *et al.* 2006) have made possible the control of rigid and flexible objects immersed in fluids on length scales smaller than the wavelength of visible light. On such scales, the hydrodynamics necessarily occurs at low Reynolds numbers and it is subject to thermal fluctuation. Under these circumstances, the proper interpretation of experimental measurements under controlled actuation relies on accurate predictions of the deterministic component of the hydrodynamics. In this paper, we focus on developing the mathematically exact, low-Reynolds-number hydrodynamic motion and tracer properties induced by spinning rods sweeping upright cones in viscous fluids. Jing (2006) has demonstrated that this type of motion can be achieved through a magnetic force microscope by synthetic rods 10 μm in length by 200 nm in cross-sectional diameter fabricated from a nickel–iron alloy. In water, the ensuing hydrodynamic interactions can move small non-magnetic micrometre-sized particles in a non-trivial fashion. This periodic actuation results in particle motion that consists of a small epicycle roughly commensurate to the rod's rotation rate, superimposed onto slow orbital motion around the precessing rod. The purpose of this paper is to present detailed theoretical predictions regarding the behaviour of such tracers as a function of their spatial location and the rod geometry (angle of inclination and slenderness).

It should be noted that besides being a technological breakthrough, such actuated controlled motions can replicate some that naturally arise in biological systems. These motions have been demonstrated to have important consequences in the early stages of foetus development in mammals (Sulik *et al.* 1994; Nonaka *et al.* 2002). In particular, Kartagener's syndrome (Kartagener 1933), an abnormal congenital condition whose symptoms range from situs inversus to infertility (Afzelius 1976), is believed to be associated with dysfunctional semirigid embryonic cilia that fail to perform motion similar to the cone-sweeping rod precession by magnetic actuation in the experiments by Jing (2006).

Motivated by these technological and biological observations, we present here the exact analytical hydrodynamic solution for a rod sweeping an upright cone while spinning on its axis in a Newtonian fluid, and study in detail the motion of passive particles advected by these complicated three-dimensional unsteady fluid flows. The solutions constructed here are built upon the singularity methods developed by Batchelor (1970), Chwang & Wu (1975), Wu (1978) and Kim (1986) stemming from the classical work of Edwardes (1892). The behaviour of the particle motion advected by these complicated fluid flows strongly depends on spatial location which we map through numerous statistics of trajectory properties.

The paper is organized as follows. In § 2, we overview the non-dimensionalizations and limiting situations we intend to study in this work. In § 3, we develop the exact hydrodynamic solution for a non-spinning rod sweeping a double upright cone in a

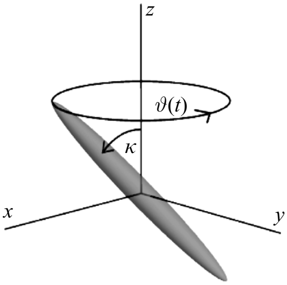

FIGURE 1. A body sweeping out a double cone.

viscous fluid. In § 4, we present the detailed trajectory properties of particles advected by this three-dimensional time-varying fluid motion. In particular, we show how rod and cone geometry greatly affects the trajectories, and present detailed statistics documenting the epicycle amplitude, arclength, angle swept per rotation and vertical fluctuation. By working in the body frame, we identify the periodic orbits that yield the epicyclic trajectories. In § 5, we discuss the flow properties, paying specific attention to documenting the local fluid speed relative to rod orientation. In § 6, we present two far-field asymptotic expressions of the flow and analyse the fluid particle dynamics in the limit of large spherical radius. We demonstrate an explicit invariant of the three-dimensional time-varying system in this limit which holds for small cone angles, as well as an invariant for arbitrary cone angles at large cylindrical radial distances. We present explicit formulae for the epicycle amplitude of particle trajectories in each of these far-field systems. In § 7, we show how to incorporate an additional axial rotation associated with the rod precession as it sweeps a cone in the fluid, a situation experimentally observed in some circumstances. We document particle trajectory properties with the addition of this extra spin.

2. Non-dimensional equations

The fundamental governing equations for an incompressible fluid system are given by the Navier–Stokes equations

$$\left.\begin{aligned}\frac{\partial \boldsymbol{u}}{\partial t} + \boldsymbol{u}\cdot\nabla\boldsymbol{u} &= -\frac{1}{\rho}\,\nabla p + \nu\nabla^2\boldsymbol{u},\\ \nabla\cdot\boldsymbol{u} &= 0,\end{aligned}\right\} \tag{2.1}$$

where ρ is the fluid density, $\boldsymbol{u}$ is the velocity field, p is the pressure, and ν is the kinematic viscosity of the fluid. These equations describe the conservation of momentum and mass, respectively.

The Reynolds number $Re = \ell \boldsymbol{U}/\nu$ is a non-dimensional measure of inertial forces to viscous forces where ℓ and $\boldsymbol{U}$ are characteristic length and velocity scales in the system of interest. Consider a body spinning about its midpoint sweeping out a double cone in a low-Reynolds-number fluid system. The body's motion is depicted in figure 1 where κ is the cone angle and $\vartheta(t)$ is the angle swept out by the cone at time t.

It is natural to define a characteristic time scale using the rotation rate of the body $\omega = \mathrm{d}\vartheta/\mathrm{d}t$. Another non-dimensional parameter arising in this problem, independent of the Reynolds number, is the Strouhal number $Sr = \omega\ell/\boldsymbol{U}$, relating oscillation frequency to fluid velocity. Using these characteristic scales, the Navier–Stokes equations are given in dimensionless primed variables as

$$\left.\begin{aligned} Sr\,Re\frac{\partial \boldsymbol{u}'}{\partial t'} + Re\ \boldsymbol{u}'\boldsymbol{\cdot}\nabla'\boldsymbol{u}' &= -\nabla' p' + \nabla'^2\boldsymbol{u}', \\ \nabla'\boldsymbol{\cdot}\boldsymbol{u}' &= 0, \end{aligned}\right\} \tag{2.2}$$

where the primed differential operators denote differentiation with respect to the primed variables. Let ℓ be half the length of the rotating body and define $\boldsymbol{U} = \omega\,\ell \sin\kappa$ to be the linear velocity of the body's tip so that

$$Sr\,Re = \frac{\omega\,\ell^2}{\nu}, \quad Re = \frac{\omega\,\ell^2 \sin\kappa}{\nu}. \tag{2.3}$$

For ω and ℓ fixed, $Sr\,Re \ll 1$ and $Re \ll 1$ when the viscosity ν is large, independently of cone angle κ. In this regime, the fluid equations reduce to the linear steady Stokes equations

$$\left.\begin{aligned} \nabla'^2\boldsymbol{u}' - \nabla' p' &= \boldsymbol{0}, \\ \nabla'\boldsymbol{\cdot}\boldsymbol{u}' &= 0. \end{aligned}\right\} \tag{2.4}$$

Note that the time derivative of the velocity field in the Stokes equations can be retained if $Sr\,Re \sim 1$ and $Re \ll 1$. For fixed ℓ and large ν, this implies that ω is large to maintain $\omega\ell^2/\nu \sim 1$. The low-Reynolds-number assumption with these large rotation frequencies ω can still be achieved when $\sin\kappa \ll 1$. Hence, in the regime of large rotation rates and small cone angles, the unsteady Stokes equations should be considered.

In this paper, we examine fluid motion dictated by the steady Stokes equations.

3. An exact solution

Edwardes (1892) examined the motion of a viscous liquid owing to an ellipsoid rotating about one of its axes. The exact solution was found through the use of ellipsoidal coordinates. To demonstrate the 'power of the singularity method', Chwang & Wu (1975) derived Stokes solutions for a prolate spheroid embedded in uniform and certain linear flows using singularity theory. (A spheroid is an ellipsoid with two of its axes equal.) Their objective was to build a collection of solutions by distributing fundamental singularities along the interior centreline of the spheroid between its foci. The description of the velocity field was given as a line integral of singularities with the appropriate strengths. Wu (1978) and Kim (1986) recast the more general ellipsoidal solutions of Edwardes as singularity solutions by distributing singularities on the interior of the fundamental ellipse of the ellipsoid. The result is a surface integral for the velocity field which collapses to the line integrals of Chwang & Wu in the case of a prolate spheroid. To obtain the fluid motion due to a body spinning about its midpoint sweeping out a cone, we adopt the strategy of Chwang & Wu. We let our body be a prolate spheroid and impose a line distribution of singularities on the centre of the spheroid between the foci. The superposition is constructed so that the motion of sweeping out a cone is achieved.

3.1. *From the body frame to the laboratory frame*

Throughout this work, we will be describing fluid motion with respect to two frames of reference, one fixed with the laboratory and one rotating with the body, respectively. In the laboratory frame, the body would appear to be rotating, sweeping out a cone in a background flow that is otherwise at rest. In the rotating, or body, frame, the body would appear to be at rest and embedded in some rotating background flow.

Chwang & Wu (1975) considered a prolate spheroid centred at the origin,

$$\frac{x^2}{a^2} + \frac{y^2 + z^2}{b^2} = 1 \qquad (a > b), \tag{3.1}$$

embedded in the free-stream linear flow $\boldsymbol{U}(\boldsymbol{x}) = \omega(y, -x, 0)$. The focal length $2c$ and eccentricity e of the spheroid are related by

$$c = \sqrt{a^2 - b^2} = ea. \tag{3.2}$$

If we define $\delta = b/a$ to be a measure of the spheroid's slenderness, then the eccentricity is expressed as $e = \sqrt{1 - \delta^2}$. Now for $\boldsymbol{x}_0$ on the boundary of this spheroid, the velocity field $\boldsymbol{u}(\boldsymbol{x})$ whose solution satisfies

$$\left.\begin{aligned} \boldsymbol{u}(\boldsymbol{x}_0) &= \boldsymbol{0}, \\ \lim_{\boldsymbol{x}\to\infty} \boldsymbol{u}(\boldsymbol{x}) &= \boldsymbol{U}(\boldsymbol{x}), \end{aligned}\right\} \tag{3.3}$$

was provided by Chwang & Wu through a distribution of Stokes doublets and point-source quadrupoles placed on the interior centreline of the spheroid between its foci. The solution to this boundary-value problem is one in which the body is fixed in a rotating background flow since $\boldsymbol{U}(\boldsymbol{x}) = -\omega(\boldsymbol{e}_z \times \boldsymbol{x})$ represents clockwise rotation of the (x, y)-plane with rate ω where $\boldsymbol{e}_z = (0, 0, 1)$ is oriented in the positive z-direction.

We are interested in the velocity solution for the motion induced in a fluid otherwise at rest by a rigid body rotating around some axis. We would like to construct such a solution through linear transformations of the appropriate body-frame solutions built by Chwang & Wu. We will consider the transformations defined by the matrices

$$\boldsymbol{R}_\kappa = \begin{pmatrix} \sin\kappa & 0 & -\cos\kappa \\ 0 & 1 & 0 \\ \cos\kappa & 0 & \sin\kappa \end{pmatrix}, \quad \boldsymbol{R}_\vartheta = \begin{pmatrix} \cos\vartheta(t) & -\sin\vartheta(t) & 0 \\ \sin\vartheta(t) & \cos\vartheta(t) & 0 \\ 0 & 0 & 1 \end{pmatrix}, \tag{3.4}$$

where $\boldsymbol{R}_\kappa$ is a steady clockwise rotation of the (x, z)-plane through an angle κ and $\boldsymbol{R}_\vartheta$ is a time-dependent counterclockwise rotation of the (x, y)-plane through an angle $\vartheta(t)$.

Suppose we can construct a velocity field $\boldsymbol{u}(\boldsymbol{x})$ in the body frame satisfying

$$\left.\begin{aligned} \boldsymbol{u}(\boldsymbol{x}_0) &= \boldsymbol{0}, \\ \lim_{\boldsymbol{x}\to\infty} \boldsymbol{u}(\boldsymbol{x}) &= R_\kappa^T \boldsymbol{U}(R_\kappa \boldsymbol{x}), \end{aligned}\right\} \tag{3.5}$$

where $\boldsymbol{x}_0$ lies on the boundary of spheroid defined in (3.1). Then the change of variables

$$\boldsymbol{x}^*(t) = R_\vartheta R_\kappa \boldsymbol{x} \tag{3.6}$$

provides a velocity field in the rotated $\boldsymbol{x}^*$-coordinate system as

$$\begin{aligned} \boldsymbol{u}^*(\boldsymbol{x}^*) &= \frac{\mathrm{d}\boldsymbol{x}^*}{\mathrm{d}t} \\ &= \left.\frac{d(R_\vartheta R_\kappa \boldsymbol{x})}{\mathrm{d}t}\right|_{\boldsymbol{x}=R_\kappa^T R_\vartheta^T \boldsymbol{x}^*} \\ &= \left.\left(\dot{R}_\vartheta R_\kappa \boldsymbol{x} + R_\vartheta R_\kappa \frac{\mathrm{d}\boldsymbol{x}}{\mathrm{d}t}\right)\right|_{\boldsymbol{x}=R_\kappa^T R_\vartheta^T \boldsymbol{x}^*} \\ &= -\boldsymbol{U}(\boldsymbol{x}^*) + R_\vartheta R_\kappa \boldsymbol{u}\left(R_\kappa^T R_\vartheta^T \boldsymbol{x}^*\right). \end{aligned} \tag{3.7}$$

At each time t, this change of variables provides a tilted rotating spheroid whose boundary is found at

$$\frac{((x\sin\kappa - z\cos\kappa)\cos\vartheta(t) - y\sin\vartheta(t))^2}{a^2} + \frac{((x\sin\kappa - z\cos\kappa)\sin\vartheta(t) + y\cos\vartheta(t))^2 + (x\cos\kappa + z\sin\kappa)^2}{b^2} = 1. \quad (3.8)$$

Assume we can solve the body-frame problem in (3.5) and let $\boldsymbol{x}_0^*$ lie on the boundary of the tilted rotating body in (3.8). Then the construction of a solution which satisfies the boundary conditions

$$\left.\begin{aligned} \boldsymbol{u}^*(\boldsymbol{x}_0^*) &= -\boldsymbol{U}(\boldsymbol{x}_0^*), \\ \lim_{\boldsymbol{x}^*\to\infty} \boldsymbol{u}^*(\boldsymbol{x}^*) &= \boldsymbol{0}, \end{aligned}\right\} \quad (3.9)$$

is verified by the velocity field (3.7) where the change of variables (3.5) guarantees that

$$\begin{aligned} \lim_{\boldsymbol{x}^*\to\infty} \boldsymbol{u}^*(\boldsymbol{x}^*) &= \lim_{\boldsymbol{x}^*\to\infty} \left(-\boldsymbol{U}(\boldsymbol{x}^*) + R_\vartheta R_\kappa \boldsymbol{u}\left(R_\kappa^T R_\vartheta^T \boldsymbol{x}^*\right)\right) \\ &= -\boldsymbol{U}(\boldsymbol{x}^*) + R_\vartheta \boldsymbol{U}\left(R_\vartheta^T \boldsymbol{x}^*\right) \\ &= \boldsymbol{0}. \end{aligned} \quad (3.10)$$

The boundary condition in (3.9) coupled with the Stokes equations describes the velocity field $\boldsymbol{u}^*(\boldsymbol{x}^*)$ due to the rigid-body motion of a spheroid tilted in the (x^*, z^*)-plane by an angle κ rotating in the (x^*, y^*)-plane sweeping out a double cone in a low-Reynolds-number fluid which is otherwise at rest. A more detailed description of the solution procedure leading to the body-frame boundary conditions of (3.5) is provided in Appendix B. Thus, obtaining the fluid motion in the laboratory frame of reference has been reduced to the solution of the auxiliary problem in the body frame of reference defined by (3.5).

3.2. *Solution to an auxiliary problem*

Define $\boldsymbol{e}_x = (1, 0, 0)$, $\boldsymbol{e}_y = (0, 1, 0)$, and $\boldsymbol{e}_z = (0, 0, 1)$ to be basis elements of $\mathbb{R}^3$ and solve Stokes equations with the linear flow

$$\begin{aligned} R_\kappa^T \boldsymbol{U}(R_\kappa \boldsymbol{x}) &= \omega \begin{pmatrix} y\sin\kappa \\ -x\sin\kappa + z\cos\kappa \\ -y\cos\kappa \end{pmatrix} \\ &= \omega(y\sin\kappa\ \boldsymbol{e}_x - x\sin\kappa\ \boldsymbol{e}_y + z\cos\kappa\ \boldsymbol{e}_y - y\cos\kappa\ \boldsymbol{e}_z), \end{aligned} \quad (3.11)$$

past the prolate spheroid in (3.1). Here, we have defined $\omega \equiv \dot{\vartheta}$ (the vertical component of the angular velocity of the body). Let $\boldsymbol{x}_0$ lie on the boundary of this spheroid and, through the linearity of Stokes equations, construct the velocity field as the sum of four contributions

$$\boldsymbol{u}(\boldsymbol{x}) = \boldsymbol{u}^1(\boldsymbol{x}) + \boldsymbol{u}^2(\boldsymbol{x}) + \boldsymbol{u}^3(\boldsymbol{x}) + \boldsymbol{u}^4(\boldsymbol{x}), \quad (3.12)$$

where $\boldsymbol{u}^i(\boldsymbol{x}_0) = 0$ for $i = 1, 2, 3, 4$ and

$$\lim_{\boldsymbol{x}\to\infty} \boldsymbol{u}^1(\boldsymbol{x}) = \omega\ y\sin\kappa \boldsymbol{e}_x, \quad (3.13a)$$

$$\lim_{\boldsymbol{x}\to\infty} \boldsymbol{u}^2(\boldsymbol{x}) = -\omega\ x\sin\kappa \boldsymbol{e}_y, \quad (3.13b)$$

$$\lim_{\boldsymbol{x}\to\infty} \boldsymbol{u}^3(\boldsymbol{x}) = \omega\ z\cos\kappa \boldsymbol{e}_y, \quad (3.13c)$$

$$\lim_{\boldsymbol{x}\to\infty} \boldsymbol{u}^4(\boldsymbol{x}) = -\omega\ y\cos\kappa \boldsymbol{e}_z. \quad (3.13d)$$

As stated above, the singularity method has been used by Chwang & Wu (1975) to solve Stokes problems exactly for prolate spheroids embedded in certain linear flows. In particular, they provide solutions for the boundary-value problems in (3.13*a*), (3.13*b*) and (3.13*c*) by distributing Stokes doublets quadratically between the foci of the spheroid and point-source quadrupoles quartically. These solutions are given in Appendix C. To complete the description for $\boldsymbol{u}(\boldsymbol{x})$, the singularity distribution for $\boldsymbol{u}^4(\boldsymbol{x})$ in (3.13*d*) must be determined. This solution is obtained from $\boldsymbol{u}^3(\boldsymbol{x})$ through the transformation $y \leftrightarrow z$ with details also provided in Appendix C.

Assembling all the pieces results in the Stokes solution

$$\begin{aligned}\boldsymbol{u}(\boldsymbol{x}) &= R_\kappa^T \boldsymbol{U}(R_\kappa \boldsymbol{x}) \\ &\quad + \omega \sin\kappa \left(\int_{-c}^{c} (c^2 - s^2)[\alpha \boldsymbol{u}_{SS}(\boldsymbol{x} - \boldsymbol{s}\,; \boldsymbol{e}_x, \boldsymbol{e}_y) + \widetilde{\gamma}_1 \boldsymbol{u}_R(\boldsymbol{x} - \boldsymbol{s}\,; \boldsymbol{e}_z)]\,\mathrm{d}s \right. \\ &\quad \left. + \ \beta \int_{-c}^{c} (c^2 - s^2)^2 \frac{\partial}{\partial y} \boldsymbol{u}_D(\boldsymbol{x} - \boldsymbol{s}\,; \boldsymbol{e}_x)\,\mathrm{d}s \right) \\ &\quad + \omega\ \widetilde{\gamma}_2\ \cos\kappa \int_{-c}^{c} (c^2 - s^2)\,\boldsymbol{u}_R(\boldsymbol{x} - \boldsymbol{s}, \boldsymbol{e}_x)\,\mathrm{d}s, \end{aligned} \tag{3.14}$$

which satisfies the body-frame problem in (3.5) where $R_\kappa^T \boldsymbol{U}(R_\kappa \boldsymbol{x})$ is given in (3.11) and

$$\widetilde{\gamma}_1 = \frac{2 - e^2}{-2e + (1 + e^2)\log\left(\dfrac{1+e}{1-e}\right)}, \tag{3.15a}$$

$$\widetilde{\gamma}_2 = \frac{1 - e^2}{2e - (1 - e^2)\log\left(\dfrac{1+e}{1-e}\right)}, \tag{3.15b}$$

$$\alpha = \frac{e^2}{-2e + (1 + e^2)\log\left(\dfrac{1+e}{1-e}\right)}, \tag{3.15c}$$

$$\beta = \frac{1 - e^2}{4\left(-2e + (1 + e^2)\log\left(\dfrac{1+e}{1-e}\right)\right)}. \tag{3.15d}$$

The notation in (3.14) is chosen to reflect that the singularities required to solve this boundary-value problem are precisely the so-called stresslet $\boldsymbol{u}_{SS}$, the rotlet $\boldsymbol{u}_R$, and a derivative of the point-source dipole $\boldsymbol{u}_D$. An account of these fundamental solutions to Stokes equations is provided in Appendix A. The solution in (3.14) and (3.15) to the auxiliary problem provides the velocity field induced by a prolate spheroid sweeping out a double cone with angle κ in an infinite viscous fluid through the transformation of (3.7).

We remark that the solution for $\boldsymbol{u}^1(\boldsymbol{x})$ contains distributions of $\partial \boldsymbol{u}_D(\boldsymbol{x}, \boldsymbol{e}_x)/\partial y$ while $\boldsymbol{u}^2(\boldsymbol{x})$ contains distributions of $\partial \boldsymbol{u}_D(\boldsymbol{x}, \boldsymbol{e}_y)/\partial x$. However, by nature of the point-source dipole, $\partial \boldsymbol{u}_D(\boldsymbol{x}, \boldsymbol{e}_x)/\partial y = \partial \boldsymbol{u}_D(\boldsymbol{x}, \boldsymbol{e}_y)/\partial x$ and only one derivative of the point-source dipole enters into the solution of (3.5). Further, the integrals in (3.14) can each be expressed in closed algebraic or logarithmic form providing an exact three-dimensional time-varying hydrodynamic solution. These expressions are presented explicitly in Appendix D.

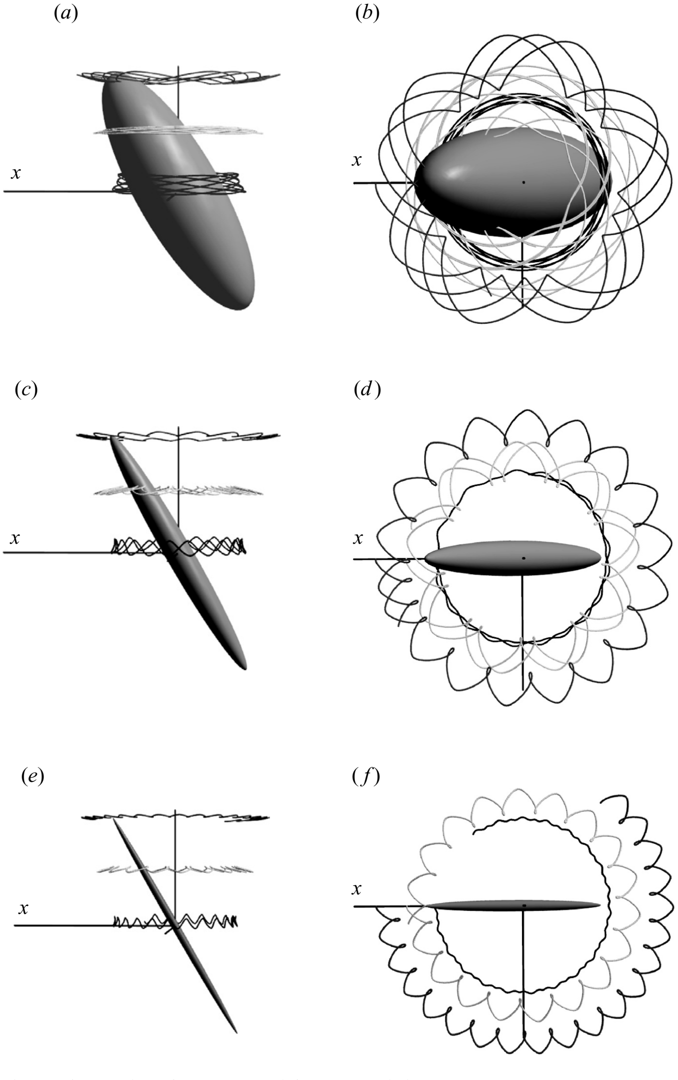

FIGURE 2. Particle trajectories for spheroid eccentricities $e = 0.95$, 0.995, 0.9995 (varying from top to bottom) for cone angle $\kappa = 30^\circ$ after 20 rod revolutions. The initial particle positions are provided in (4.4). The corresponding top view is shown to the right. The spheroid rotates in the counterclockwise direction.

4. Trajectory properties

The particle trajectory $\boldsymbol{x}^* = (x^*(t), y^*(t), z^*(t))$ for a tracer moving passively in the presence of this fluid flow must be computed numerically from the system of non-autonomous ordinary differential equations

$$\frac{\mathrm{d}\boldsymbol{x}^*}{\mathrm{d}t} = \boldsymbol{u}^*(\boldsymbol{x}^*(t), t), \tag{4.1}$$

where $\boldsymbol{u}^*(\boldsymbol{x}^*)$ is provided by (3.7) and (3.14). A typical series of trajectories of the exact solution are depicted in figures 2 and 3 for the cone angles $\kappa = 30^\circ$ and 60° and varying spheroid eccentricities e when the rotation rate of sweeping out a cone is

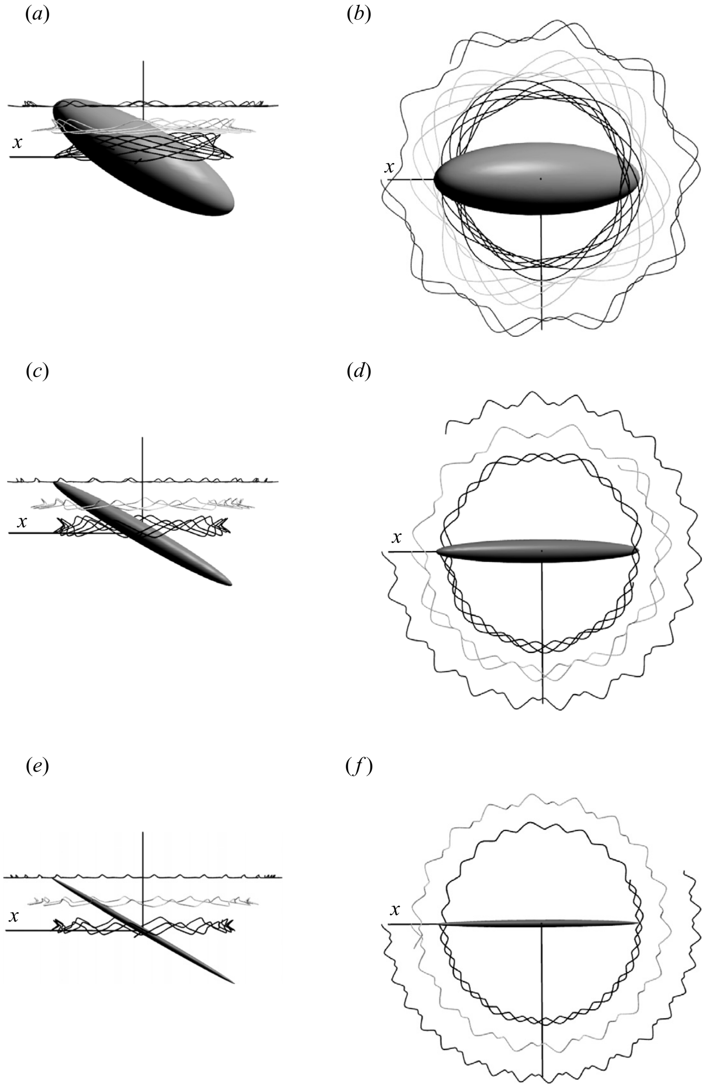

FIGURE 3. Particle trajectories for spheroid eccentricies $e = 0.95$, 0.995, 0.9995 (varying from top to bottom) for cone angle $\kappa = 60^\circ$ after 20 rod revolutions. The initial particle positions are provided in (4.4). The corresponding top view is shown to the right.

(throughout this section unless otherwise indicated) $\omega = 2\pi$. The eccentricities shown relate to the slenderness δ defined in § 3.1 by

$$\left.\begin{aligned} e = 0.95 &\Longrightarrow \delta \approx 0.31225,\\ e = 0.995 &\Longrightarrow \delta \approx 0.09987,\\ e = 0.9995 &\Longrightarrow \delta \approx 0.03162, \end{aligned}\right\} \qquad (4.2)$$

which can be seen qualitatively in the figures. Initially, the upper tip of the rod is located at $(\sin\kappa, 0, \cos\kappa)$. These same values define a cone radius CR and a cone height CH

$$\mathrm{CR} = \sin\kappa, \quad \mathrm{CH} = \cos\kappa. \qquad (4.3)$$

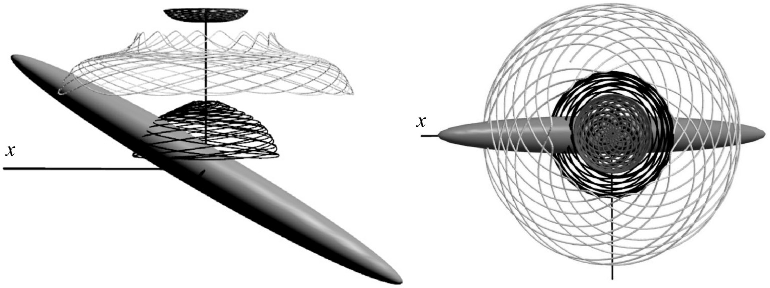

FIGURE 4. Particle trajectories for spheroid eccentricity $e = 0.995$ and cone angle $\kappa = 60°$ after 20 rod revolutions for the initial positions in (4.6) placed within the cone structure defined by (4.5). The corresponding top view is shown to the right. The spheroid rotates in the counterclockwise direction.

For each set of κ and e in figures 2 and 3, trajectories for the initial positions

$$\boldsymbol{x}^*(0) = \begin{cases} (1.5\,\mathrm{CR}, 0, \mathrm{CH}) \\ (1.25\,\mathrm{CR}, 0, 0.5\,\mathrm{CH}) \\ (\mathrm{CR}, 0, 0) \end{cases} \tag{4.4}$$

after 20 rod revolutions computed using fourth-order Runge–Kutta with 10^4 time steps per rotation on the exact velocity field are shown. The numerical algorithm is provided by Leiterman (2006) as a Fortran 77 code. Each of the initial conditions in (4.4) starts outside the cone structure centred about

$$x^2 + y^2 = z^2 \tan^2 \kappa \tag{4.5}$$

which has a thickness corresponding to the radius of the tilted spheroid at a given height. Figure 4 shows trajectories for cone angle $\kappa = 60°$ and eccentricity $e = 0.995$ for the initial positions

$$\boldsymbol{x}^*(0) = \begin{cases} (0, 0, 0.65\,\mathrm{CH}) \\ (-0.3\,\mathrm{CR}, 0, 0.6\,\mathrm{CH}) \\ (-0.05\,\mathrm{CR}, 0, 0.3\,\mathrm{CH}) \end{cases} \tag{4.6}$$

interior to this cone structure. The trajectories in figures 2, 3 and 4 exhibit two oscillations. A faster fluctuation related to the rotation rate of the spheroid and a distance dependent slower cycle.

The faster fluctuation is an epicycle which has a polar amplitude and a vertical fluctuation. We define the polar amplitude of an epicycle to be the difference between the maximum and minimum

$$a_p(T) \equiv \max_{t\in[0,T]} r_\perp(t) - \min_{t\in[0,T]} r_\perp(t) \tag{4.7}$$

of the cylindrical radial coordinate

$$r_\perp(t) \equiv |\boldsymbol{x}_\perp^*(t)| = \sqrt{x^*(t)^2 + y^*(t)^2}$$

over a interval of time $[0, T]$ in the laboratory frame. The vertical fluctuation is similarly regarded as the difference between the maximum and minimum of the vertical component $z^*(t)$ of a trajectory. Polar amplitude and vertical fluctuation each decrease with increasing eccentricity, or increasing slenderness, which can be observed in the sequence of graphs in figures 2 and 3. Each epicycle also travels an angular distance contributing to the slower oscillation of the trajectory in which a fluid particle makes a complete revolution about the spheroid. This orbital period is distance dependent and also decreases with increasing eccentricity.

The period of an epicycle is, in general, not commensurate with spheroid rotation rate. Figure 5 shows the path of fluid particles after consecutive integer spheroid revolutions for initial positions which vary from inside to outside the cone at a fixed height. These paths are shown for cone angles $\kappa = 30^\circ$ and 60° and eccentricity $e = 0.995$. The trajectory of a particle after three rod revolutions would be the superposition of each of the three paths shown in figure 5. The spheroid sweeps out a double cone so that any particle initialized on the spheroid's surface has a circular trajectory. The grey region in the figure represents the annulus swept out by the spheroid at $z^* = z_0$ which is bounded by such circular trajectories.

4.1. *A body-frame generator*

We have thus far constructed a three-dimensional time-varying flow field in the laboratory frame. The resulting trajectories are also three-dimensional and time varying. Consider the change of variables

$$\boldsymbol{x}' = R_\vartheta^T \boldsymbol{x}^*, \tag{4.8}$$

where R_ϑ^T is the transpose of the time-varying rotation in (3.4). The velocity field in the $\boldsymbol{x}'$-coordinate system becomes

$$\begin{aligned}
\boldsymbol{u}'(\boldsymbol{x}') &= \frac{\mathrm{d}\boldsymbol{x}'}{\mathrm{d}t} \\
&= \left.\frac{\mathrm{d}\left(R_\vartheta^T \boldsymbol{x}^*\right)}{\mathrm{d}t}\right|_{\boldsymbol{x}^* = R_\vartheta \boldsymbol{x}'} \\
&= \dot{R}_\vartheta^T R_\vartheta \boldsymbol{x}' + R_\vartheta^T \boldsymbol{u}^*(R_\vartheta \boldsymbol{x}') \\
&= \boldsymbol{U}(\boldsymbol{x}') - R_\vartheta^T \boldsymbol{U}(R_\vartheta \boldsymbol{x}') + R_\kappa \boldsymbol{u}\left(R_\kappa^T \boldsymbol{x}'\right) \\
&= R_\kappa \boldsymbol{u}\left(R_\kappa^T \boldsymbol{x}'\right),
\end{aligned} \tag{4.9}$$

upon using the transformation in (3.7) between the laboratory-frame velocity $\boldsymbol{u}^*(\boldsymbol{x}^*)$ and the body-frame velocity $\boldsymbol{u}(\boldsymbol{x})$ of the auxiliary problem. By design of the auxiliary problem boundary conditions in (3.5), it is found that

$$\left.\begin{aligned}
\boldsymbol{u}'(\boldsymbol{x}_0') &= \boldsymbol{0}, \\
\lim_{\boldsymbol{x}' \to \infty} \boldsymbol{u}'(\boldsymbol{x}') &= \boldsymbol{U}(\boldsymbol{x}'),
\end{aligned}\right\} \tag{4.10}$$

where $\boldsymbol{x}_0'$ lies on the tilted spheroid

$$\frac{(x' \sin\kappa - z' \cos\kappa)^2}{a^2} + \frac{(y')^2 + (x' \sin\kappa + z' \cos\kappa)^2}{b^2} = 1. \tag{4.11}$$

The $\boldsymbol{x}'$-coordinate spheroid is determined by applying R_ϑ^T to the tilted rotating spheroid in (3.8). The result is a steady velocity field for a tilted spheroid embedded in the background rotation $\boldsymbol{U}(\boldsymbol{x}') = \omega\ (y', -x', 0)$. This body-frame solution differs from the body-frame solution of the auxiliary problem (3.5). In the auxiliary problem, the spheroid is not tilted, but rather lying on an axis embedded in another rotating flow, namely, $R_\kappa^T \boldsymbol{U}(R_\kappa \boldsymbol{x})$ defined by (3.11).

Through the transformation in (4.8), every trajectory in the laboratory frame can be viewed in this alternative body frame. Hence, trajectories $\boldsymbol{x}'$ can be viewed as generators of the laboratory-frame motion through an application of R_ϑ. Figure 6

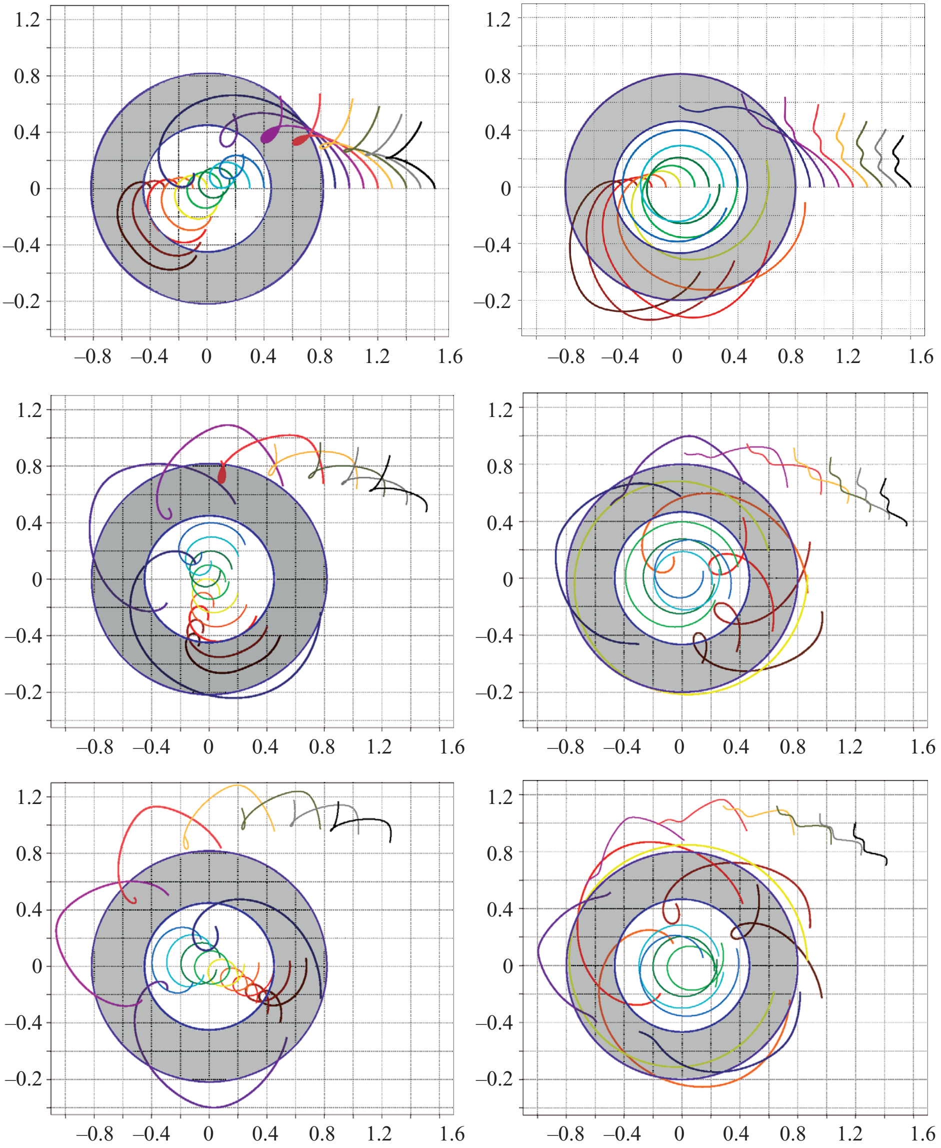

FIGURE 5. A top view of particle trajectories over consecutive spheroid revolutions for initial positions x_0 which vary from inside to outside the cone where the horizontal axis is x^* and the vertical axis is y^*. In each plot, $y_0 = 0$ and $z_0 = 0.65\,\mathrm{CH}$. The left-hand column shows trajectories for cone angle $\kappa = 30^\circ$ while the right-hand column shows those for $\kappa = 60^\circ$. The paths are shown for spheroid revolutions 0 to 1, 1 to 2 and 2 to 3 (top to bottom). The grey region is the annulus swept out by the spheroid with eccentricity $e = 0.995$ at $z^* = z_0$. It is bounded by circular trajectories produced from particles which are initialized on the rotating body.

shows a collection of trajectories in the laboratory frame with initial conditions sampled from figure 5 and the corresponding transformed trajectories which emanate from the steady velocity field in (4.9). The same collection is shown from different perspectives. The body-frame trajectories are periodic orbits whose periods depend on initial position, cone angle and eccentricity. Each closed orbit generates an epicyclic

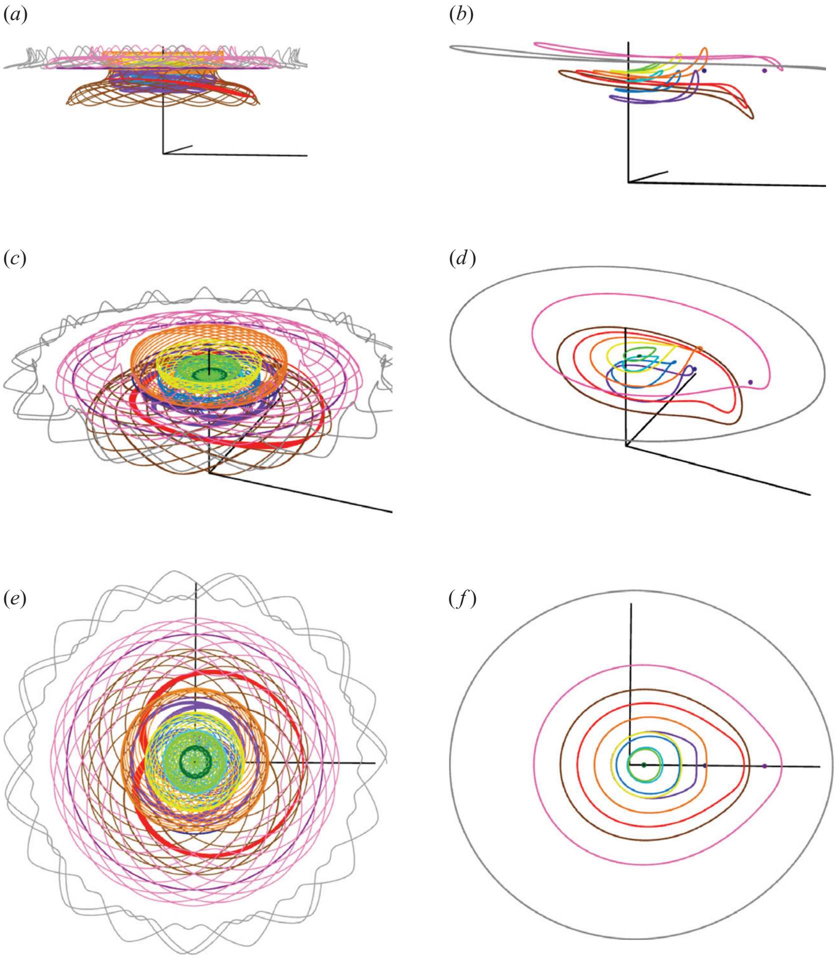

FIGURE 6. The left-hand column shows a collection of trajectories in the laboratory frame with initial conditions sampled from figure 5 for cone angle $\kappa = 60°$ and eccentricity $e = 0.995$. The corresponding body-frame trajectories formulated by (4.8) are shown on the right. This collection is given over perspectives which vary from a side to a top view after 30 spheroid revolutions. Circular trajectories in the laboratory frame resulting from particles initialized on the spheroid are seen as single points in this body frame. One orbit of a body-frame trajectory generates the epicycles seen in a laboratory frame trajectory.

trajectory when seen in the laboratory frame. Trajectory properties, such as polar amplitude and vertical fluctuation, can be measured in either the laboratory or this body frame of reference. We remark that, in general, the difference between the maximum and minimum of the cylindrical radial coordinates of a generator will correspond to the amplitude (of the (x, y)-projection) of an epicycle, i.e.

$$a_e \equiv \max_T a_p(T), \tag{4.12}$$

according to the definition (4.7) of polar amplitude.

Next, examine the generators in figure 6 more closely. In the perspective provided by figure 6(a), there is a transition between the orange and the red trajectories in which the orange trajectory curls up while the red one curls down. This transition

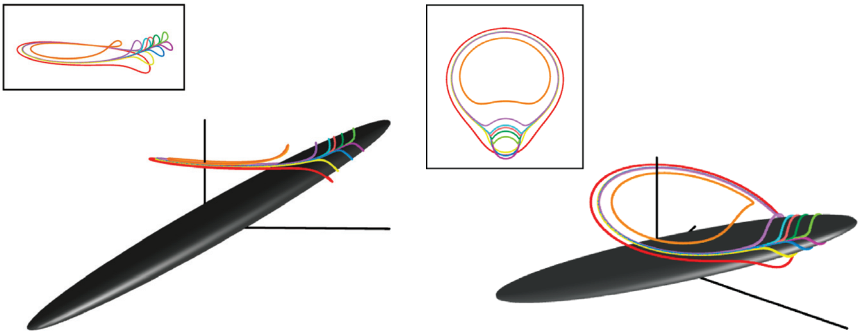

FIGURE 7. Body-frame orbits which climb and wrap the spheroid for cone angle $\kappa = 60°$, eccentricity $e = 0.995$ and initial position $(x_0\,\mathrm{CR}, 0, 0.65\,\mathrm{CH})$ over two perspectives. The values of x_0 are provided in the caption of figure 8 and vary between $-0.3\,\mathrm{CR}$ and $-0.2\,\mathrm{CR}$. The insets show two different perspectives of the same orbits but with the body omitted, (*a*) from a generic viewpoint to the side and (*b*) from a top viewpoint along the z-axis.

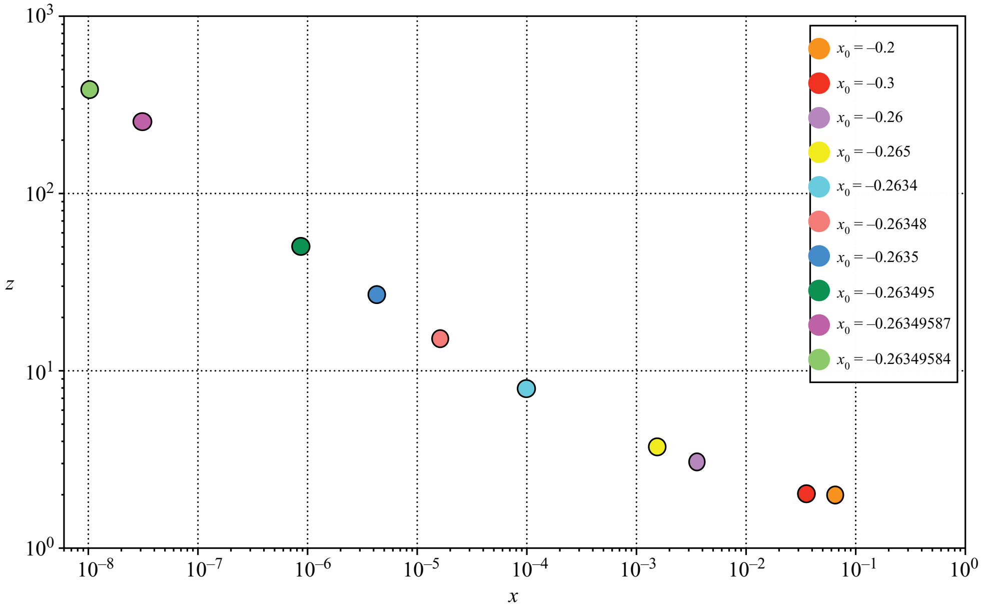

FIGURE 8. The number of spheroid revolutions required for the body-frame orbits in figure 7 (related by colour) to close as a log–log plot against the difference in initial position x_0 between a given trajectory and that of the trajectory from $x_0 = -0.26349584\mathrm{CR}$ which climbs farthest up the rod. Trajectories which are initialized to the left of $x_0 = -0.26349584\mathrm{CR}$ have orbits which wrap around the backside of the spheroid hence containing it whereas those that are initialized to the right of this value have orbits which wrap the frontside of the spheroid and do not enclose the body.

is illustrated more clearly in figure 7 which includes the position of the spheroid in this body frame of reference. The transition between the curling up and curling down includes orbits in which a particle decides to route around the spheroid enclosing it or pass in front of it. This decision is dictated by a particle's initial position. Figure 7 shows the same body-frame trajectories over varying perspectives. The intermediate trajectory between hugging the front of the body or wrapping around it must be one which climbs all the way to the tip of the spheroid (and descends on the other side). This trajectory is not depicted in figure 7. The initial position of the trajectory which climbs the furthest to the tip is $x_0 = -0.26349584\,\mathrm{CR}$. This orbit closes after 385.678 spheroid revolutions, whereas the trajectory which has an initial position of $x_0 = -0.26348\,\mathrm{CR}$ closes after just 15.179 revolutions. The period of each of the trajectories in figure 7 is plotted in figure 8. The reason for the large increase in orbital period over small changes in initial position is that the initial position determines how close the particle approaches to the surface of the spheroid. This surface, because of the no-slip boundary condition on the velocity field, can be viewed as a manifold of fixed points, and so orbits that approach any of its neighbourhoods must have small velocities, thereby taking a long time to leave the neighbourhood and hence resulting in a large contribution to the time period. This mechanism for time period increase is reminiscent of that observed in dynamical systems theory for periodic orbits approaching a hyperbolic fixed point, where such a phenomenon plays a significant role in creating the conditions for chaotic particle trajectories (for three-dimensional Stokes flow-specific examples, see e.g. Bajer & Moffatt 1990; Stone, Nadim & Strogatz 1991; Kroujiline & Stone 1999). However, because of the degeneracy of the entire spheroid surface being a set of fixed points, there are significant differences with respect to the usual hyperbolic case treated in the literature. In particular, the numerical evidence in figure 7 shows that chaotic motion is not likely under the boundary conditions we have examined, and the entire fluid space, viewed in the body reference frame, seems to be spanned solely by periodic orbits. It may be of interest to classify the fluid particle motion for this exact solution of three-dimensional Stokes flows (as opposed to approximate ones, such as those for the fluid droplets considered in studies mentioned above, where the droplet's free-surface deformation away from spherical is ignored). However, a thorough study of the fluid particle kinematics for the present set-up, and, in particular, of the role that its discrete symmetries play in the complete integrability of the particle trajectories, is beyond the scope of this paper and will be presented elsewhere.

In what follows, we are going to examine four trajectory properties of this flow: polar amplitude, angle travelled, vertical fluctuation and arclength. We chose these properties having experimental situations in mind (Jing 2006), where these quantities are easy to observe and measure. Moreover, such quantities are likely to play a role in the biological implication of our study; they can be used to quantify the amount of fluid stirring caused by precessing rods, which in turn may affect the distribution of tracers in the fluid. Accordingly, we document each of these properties on trajectories in the laboratory frame of reference, which allows for direct observation without the need for moving instrumentation such as cameras and microscopes; the trajectories are then provided by the system of ordinary differential equations in (4.1).

4.2. *Polar amplitude*

As defined in (4.7), polar amplitude is regarded as the amplitude of the epicycles projected on the $z = 0$ plane. It is clear that each trajectory in this flow is determined by a cone angle κ, an eccentricity e, and an initial position (x_0, y_0, z_0). Trajectories are further defined by the integration domain which is some interval in time. Recall that the spheroid is initially oriented in the $y = 0$ plane with its upper tip in the first quadrant.

Figure 9 shows a collection of colour density plots of polar amplitude. The polar amplitude shown is measured on the trajectories which result from a single spheroid

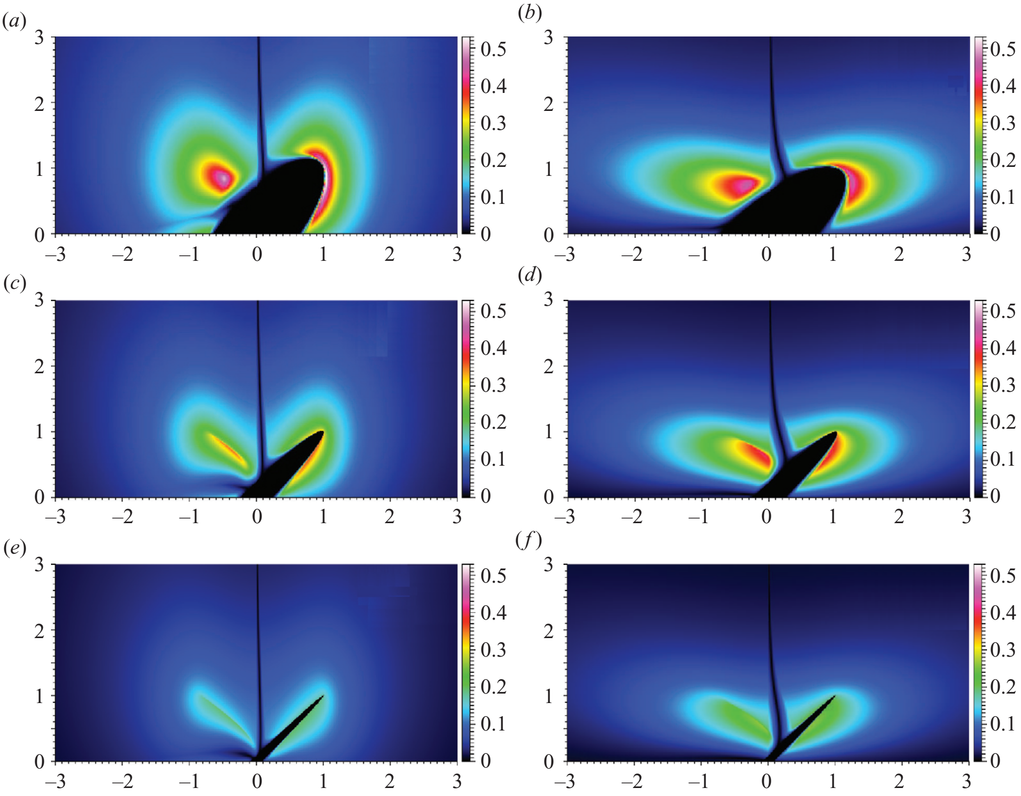

FIGURE 9. Colour density plots of polar amplitude measured on trajectories which result from a single spheroid revolution initialized at the position $(x_0, 0, z_0)$. Colour is amplitude while the horizontal axis is x_0 (measured in cone radius CR) and the vertical axis is z_0 (measured in cone height CH). The plane $y^* = 0$ intersects the spheroid which is seen as the centre black ellipsoid. Since a fluid particle cannot be initialized within the body, there are no trajectories from which amplitude can be measured in this region. The left-hand column shows amplitude for cone angle $\kappa = 30°$ while the right-hand column shows that for $\kappa = 60°$. Plots are also shown over varying eccentricities $e = 0.95, 0.995, 0.9995$ (from top to bottom).

revolution, or more precisely, on trajectories over times $0 \leqslant t < 2\pi$. For each of the plots in this figure, $y_0 = 0$. Colour represents amplitude while the horizontal axis is x_0 and the vertical axis is z_0. The set of initial conditions $(x_0, 0, z_0)$ samples a plane which intersects the spheroid. Hence, in this set there are values of x_0 and z_0 for which polar amplitude cannot be measured because they reside within the body. These regions can be seen as the black ellipsoids in figure 9.

Observe the asymmetry of polar amplitude in the upper plane. Although not illustrated in figure 9, polar amplitude is symmetric about the origin. The symmetry about the origin is expected, owing to the nature of the free-space precession of a body about its midpoint. To explain the asymmetry in the upper plane, consider the evolution of fluid particles. In figure 10, a circle of initial positions is placed in the $\theta = \pi$ plane. The spheroid revolves and when a particle intersects the $\theta = 0$ plane on integral revolutions, it is plotted. The result is the curved shaped near the upper tip of the rod on the right. The evolution of this circle to the crescent on integral spheroid revolutions indicates how the region of large amplitude on the left of figure 9 evolves to the large-amplitude region on the right (regions red-shifted in colour). In addition,

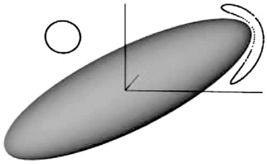

FIGURE 10. Integer time Poincaré section. A circle of initial positions is placed in the $\theta = \pi$ plane shown on the left. The spheroid revolves and when a particle intersects the $\theta = 0$ plane on integral revolutions, it is plotted. This intersection of the discretized circle shown occurs on integer revolutions which vary from 1 to 300. The result is the crescent on the right. The evolution of this circle to the crescent explains the asymmetry of polar amplitude in figure 9. Corresponding initial positions on the circle and the crescent result in the same trajectory.

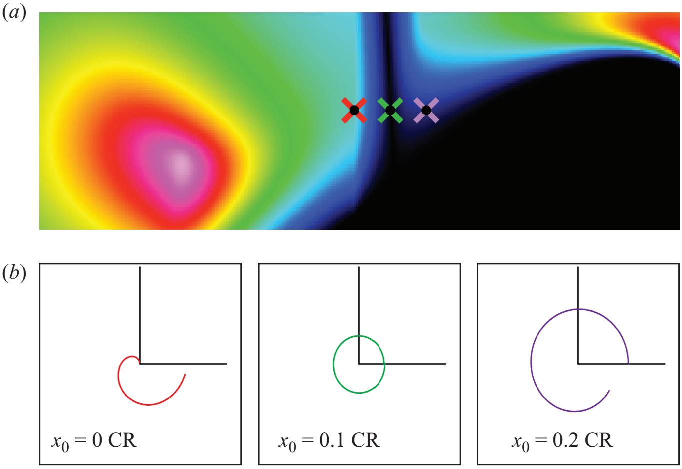

FIGURE 11. (*a*) A sample of initial conditions centred on three crosses (left to right) about $x_0 = 0$ on a colour density plot of polar amplitude. This is a magnified image of figure 9 (*a*) where $\kappa = 30°$ and $e = 0.95$. (*b*) The corresponding (left to right) trajectories after one spheroid revolution from which polar amplitude was measured.

fluid particles initialized at the corresponding position on the crescent have the same trajectory as its counterpart which was initialized on the circle. Next, examine the discontinuity about $x_0 = 0$. To explain the sharp contrast in colour, figure 11 shows trajectories for three initial positions about this zero polar amplitude strip. The trajectories presented result from a single spheroid revolution. Near-circular projected trajectories have near-zero polar amplitude. Figure 11 demonstrates a narrow region about $x_0 = 0$ of initial positions for which trajectories nearly close after one spheroid revolution.

4.3. *Angle travelled*

Another feature noted of the particle trajectories in this flow is a distance-dependent orbital period. The angle travelled by a particle per spheroid revolution contributes to the time it takes for that particle to make a complete revolution about the spheroid.

Figure 12 shows a collection of greyscale density plots of the angle travelled. This angle is measured on the trajectories which result from a single spheroid revolution as done for the colour density plots of polar amplitude in figure 9. Again, for each of the plots in this figure, $y_0 = 0$. Further, the set of initial conditions $(x_0, 0, z_0)$ samples a plane which intersects the spheroid, and these regions are seen as the black ellipsoids

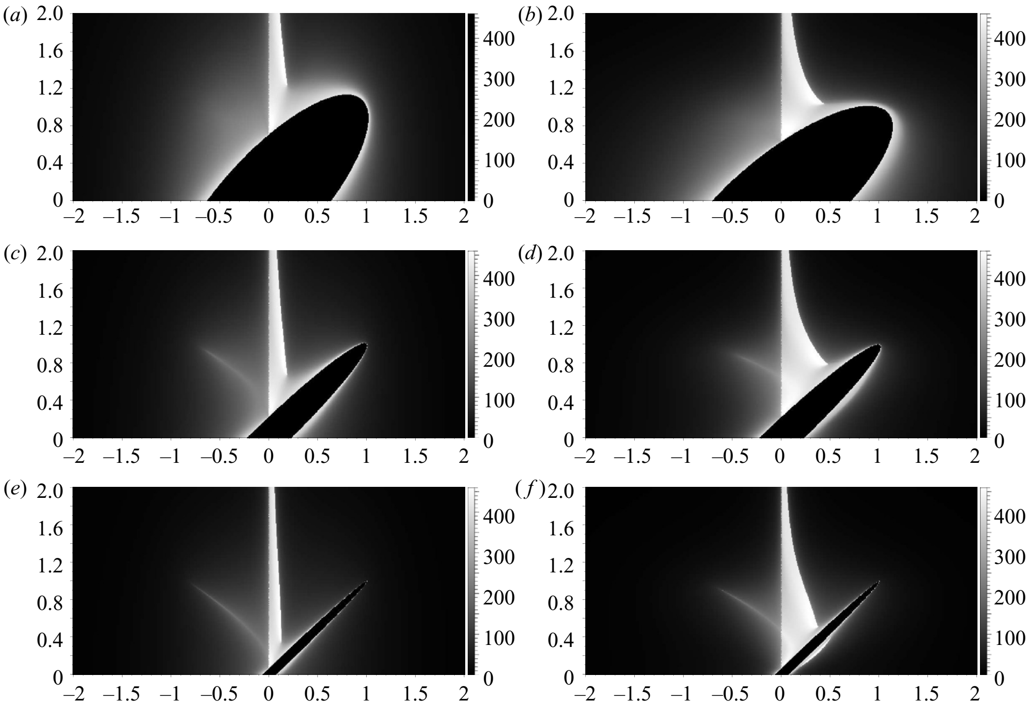

FIGURE 12. Greyscale density plots of the angle travelled by trajectories which result from a single spheroid revolution initialized at the position $(x_0, 0, z_0)$. The greyscale is the angle travelled (measure in degrees) while the horizontal axis is x_0 (measured in cone radius CR) and the vertical axis is z_0 (measured in cone height CH). The left-hand column shows the angle travelled for the cone angle $\kappa = 30°$ while the right-hand column shows that for $\kappa = 60°$. Plots are also shown for eccentricities which vary over $e = 0.95$, 0.995, 0.9995 (from top to bottom). The plane $y^* = 0$ intersects the spheroid which is seen as the centre ellipsoid from which no fluid particle can be initialized.

in figure 12. As with polar amplitude, the angle travelled is symmetric about the origin.

Observe the discontinuity near $x_0 = 0$. To explain the sharp contrast in the greyscale, figure 13 shows trajectories for four initial positions about this discontinuity where the centre and right-hand crosses of the row mark the same initial conditions as the left-hand (red) and center (green) crosses, respectively, in figure 11. The change in the greyscale of angle travelled, from dark grey to off white, corresponds to a jump of 180°. As the initial condition of a trajectory moves to $x_0 = 0$ from the left, the trajectory begins to enclose the origin. The result is a jump in the measure of the angle travelled by precisely 180°. The row of crosses are initial conditions for the first three trajectories (left to right) shown in figure 13(*b*). This enclosure of the origin, resulting in a discontinuity of the greyscale, is seen in the evolution of these three trajectories. The greyscale density plots of figure 12 also demonstrate the existence of initial conditions for which resulting trajectories travel further than 360° on a single spheroid revolution. A sample of such a trajectory is given in figure 13(*b*, far right). Regions for such behaviour are found for initial positions deep within the cone structure and also for those near the top of the cone structure at about half the cone radius.

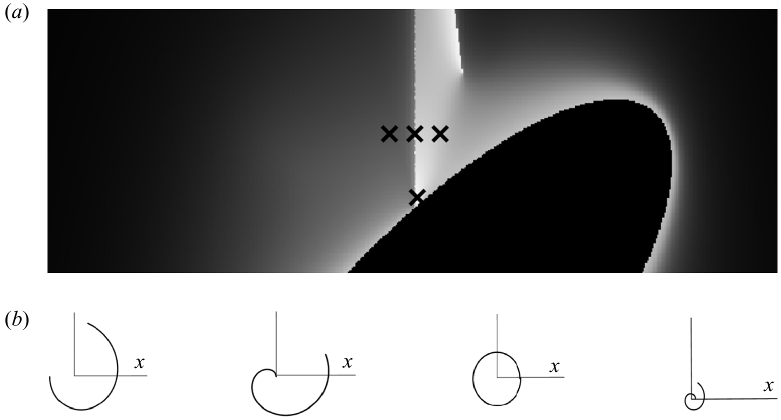

$r_0 = -0.1$ CR $r_0 = 0$ CR $r_0 = 0.1$ CR $r_0 = 0.05$ CR

FIGURE 13. (*a*) A sample of initial conditions centred on crosses in a row (left to right) about $x_0 = 0$ and one at $x_0 = 0.05$ CR deep within the cone structure on a greyscale density plot of the angle travelled. This is a magnified image of figure 12(*a*) where $\kappa = 30°$ and $e = 0.95$. (*b*) The corresponding trajectories after one spheroid revolution from which the angle travelled was measured. The first three are generated by the initial conditions in the top row of crosses (left to right) while the bottom cross is the far-right trajectory. The last two crosses of the top row are the same initial conditions as the red (left) and green (middle) crosses in figure 11.

4.4. *Vertical fluctuation*

Particle trajectories $(x^*(t), y^*(t), z^*(t))$ exhibit three-dimensional structure. The vertical fluctuation of a trajectory is regarded as the difference between the maximum and minimum of the vertical component $z^*(t)$. Figure 14 shows a collection of greyscale density plots of the vertical fluctuation. This vertical fluctuation is measured on trajectories which result from a single spheroid revolution as done for the previous density plots. Again, the vertical fluctuation is symmetric about the origin which is illustrated in this figure. Figure 14 demonstrates that the areas of largest vertical fluctuation are near $z_0 = 0$ and about the cone structure edges at $(x_0, z_0) = (\pm \text{CR}, \pm \text{CH})$.

4.5. *Arclength*

Although the arclength of a trajectory per spheroid revolution is not an indicator of orbital period, it does provide information about the structure of particle paths. For cone angle $\kappa = 30°$ and eccentricity $e = 0.95$, figure 15 displays greyscale density plots of the arclength of trajectories after a single spheroid revolution. The left-hand plot results from trajectories sampled over initial position $(x_0, 0, z_0)$. This set could be recast as $(r_0 \cos\theta_0, r_0 \sin\theta_0, z_0)$ for $\theta_0 = 0°$. Figure 15 shows greyscale density plots over the set of $\theta_0 = 0°, 30°, 60°, 90°$. Recall that the spheroid starts in the $y^* = 0$ plane with its upper tip in the first quadrant. Initiating a particle at varying θ_0 is equivalent to viewing trajectories initiated at different times since time is measured in spheroid revolutions.

5. Flow properties

5.1. *Speed*

Figure 16 displays a collection of greyscale density plots of the magnitude of the three-dimensional velocity field, or the speed, measured at $(x^*, 0, z^*)$. The greyscale

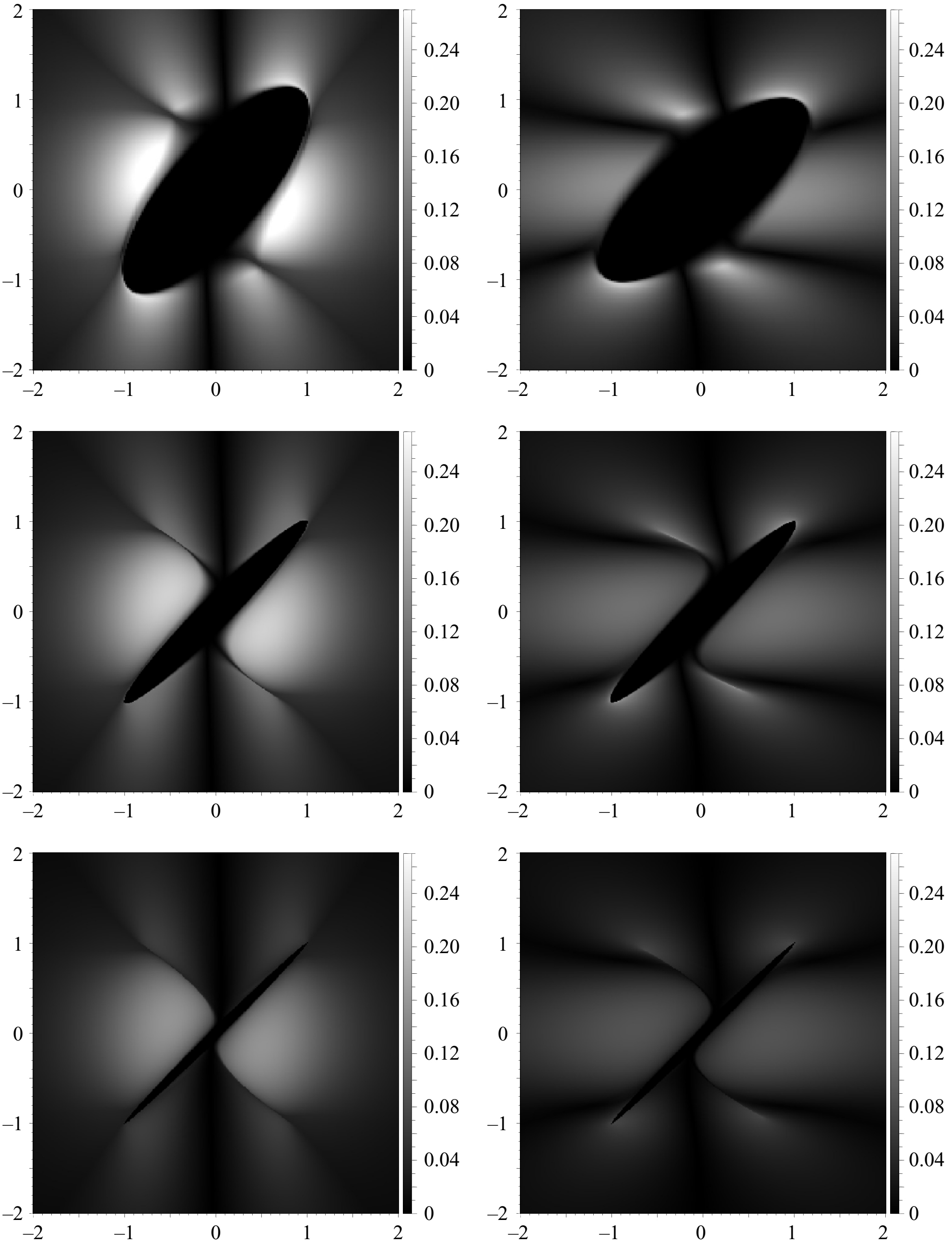

FIGURE 14. Greyscale density plots of the vertical fluctuation on trajectories which result from a single spheroid revolution initialized at the position $(x_0, 0, z_0)$. The greyscale is the vertical fluctuation while the horizontal axis is x_0 (measured in cone radius CR) and the vertical axis is z_0 (measured in cone height CH). The left-hand column shows vertical fluctuation for cone angle $\kappa = 30°$ while the right-hand column shows that for $\kappa = 30°$. Plots are also shown over eccentricities which vary over $e = 0.95$, 0.995, 0.9995 (from top to bottom). Again, the plane $y^* = 0$ intersects the spheroid which is seen as the centre ellipsoid from which no fluid particle can be initialized.

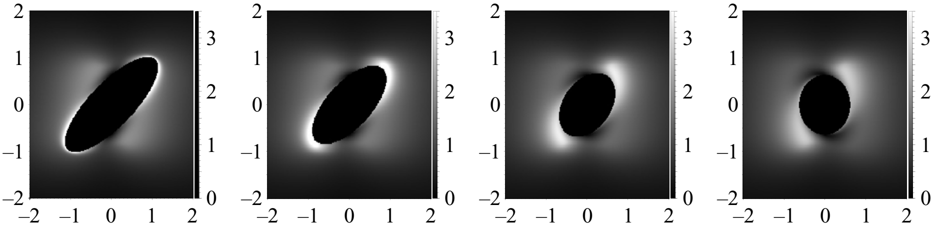

FIGURE 15. Greyscale density plots of the arclength of trajectories which result from a single spheroid revolution initialized at the position $(r_0 \cos\theta_0, r_0 \sin\theta_0, z_0)$ as a function of r_0 (horizontal axis measured in CR) and z_0 (vertical axis measured in CH) for $\theta_0 = 0°, 30°, 60°, 90°$ (left to right) when the cone angle $\kappa = 30°$ and eccentricity $e = 0.95$. By varying θ_0 and recalling that time is measured in spheroid revolutions, this figure represents a times series of arclength. As explained in the previous density plots, each fixed θ_0-plane intersects the spheroid. This is observed as the central black region from which no fluid particle can be initialized and, hence, from which arclength cannot be measured.

represents speed while the horizontal axis is x^* and the vertical axis is z^*. The set of points $(x^*, 0, z^*)$ samples a plane which intersects the spheroid. Hence, in this set, there are values of x^* and z^* for which speed is not measured because these points reside within the body and outside the fluid domain. These regions are the black ellipsoids in figure 16. As expected, the magnitude of the velocity field is largest near the tips of the spheroid.

5.2. *Cylindrical velocity components*

The velocity field can be cast into a cylindrical coordinate system

$$x^* = r\cos\theta, \quad y^* = r\sin\theta, \quad z^* = z, \tag{5.1}$$

resulting in a radial velocity u_r, azimuthal velocity u_θ and the vertical velocity of the Cartesian system u_z. Figures 17(*a*)–17(*d*) show the particle velocity, in cylindrical coordinates, as a function of time for cone angles $\kappa = 30°$ and 60° and eccentricities $e = 0.95$ and 0.995. The corresponding particle trajectories for these velocities are shown in figures 2(*a–d*) and 3(*a–d*). Figure 17(*e*, *f*) displays particle speed versus time for the velocities shown in figure 17(*a–d*).

Figure 17 demonstrates the existence of initial conditions for which local extrema in the azimuthal and vertical velocity emerge over varying cone angle and eccentricity. In figure 17(*a–d*), the solid and dotted curves, at fixed eccentricity but varying cone angle, have different numbers of local extrema per cycle. The emergence of local extrema in particle speed is also observed as cone angle and eccentricity varies. This is clear from figure 17(*e*, *f*). Figure 17(*e*) has a fixed cone angle while the solid curves across figures 17(*e*) and 17(*f*) have a fixed eccentricity.

It is worth noting that at the centre of the maximal regions in speed, the body and particle are aligned in a particular way, namely, the angular positions of the particle and spheroid tip (the end in the half-space of particle initialization) are the same. Thus, at this time, the particle and spheroid are said to be aligned. During alignment, speed can take a maximal value or it can assume a local minimum centred between maximal values. This is demonstrated in figure 17(*e*). Moreover, at the centre of the minimal regions in speed, the body and particle are said to be anti-aligned. That is, the angular positions of the particle and spheroid tip differ by 180°. Much like alignment, anti-alignment may occur at either local or global minima in speed which may or may not be surrounded by local extrema. This is observed in the solid curves

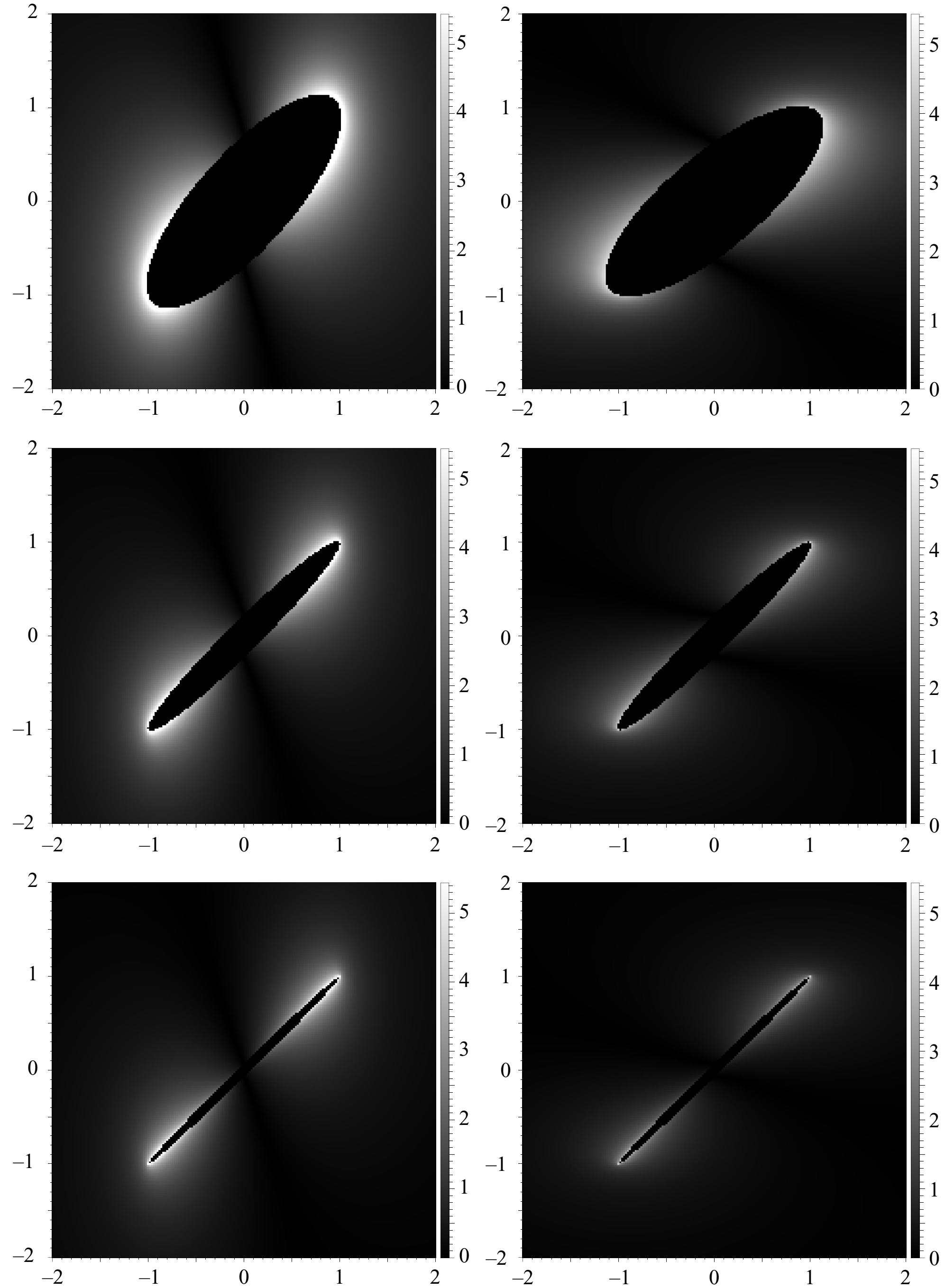

FIGURE 16. Greyscale density plots of the magnitude of the velocity field, or the speed, measured at the points $(x^*, 0, z^*)$. The greyscale is speed while the horizontal axis is x^* (measured in cone radius CR) and the vertical axis is z^* (measured in cone height CH). The left-hand column shows speed for cone angle $\kappa = 30°$ while the right-hand column shows that for $\kappa = 60°$. Plots are also shown over varying eccentricities $e = 0.95, 0.995, 0.9995$ (from top to bottom). The plane $y^* = 0$ intersects the spheroid which is seen as the centre ellipsoid. No fluid particles reside in this region and, hence, speed is not measured here.

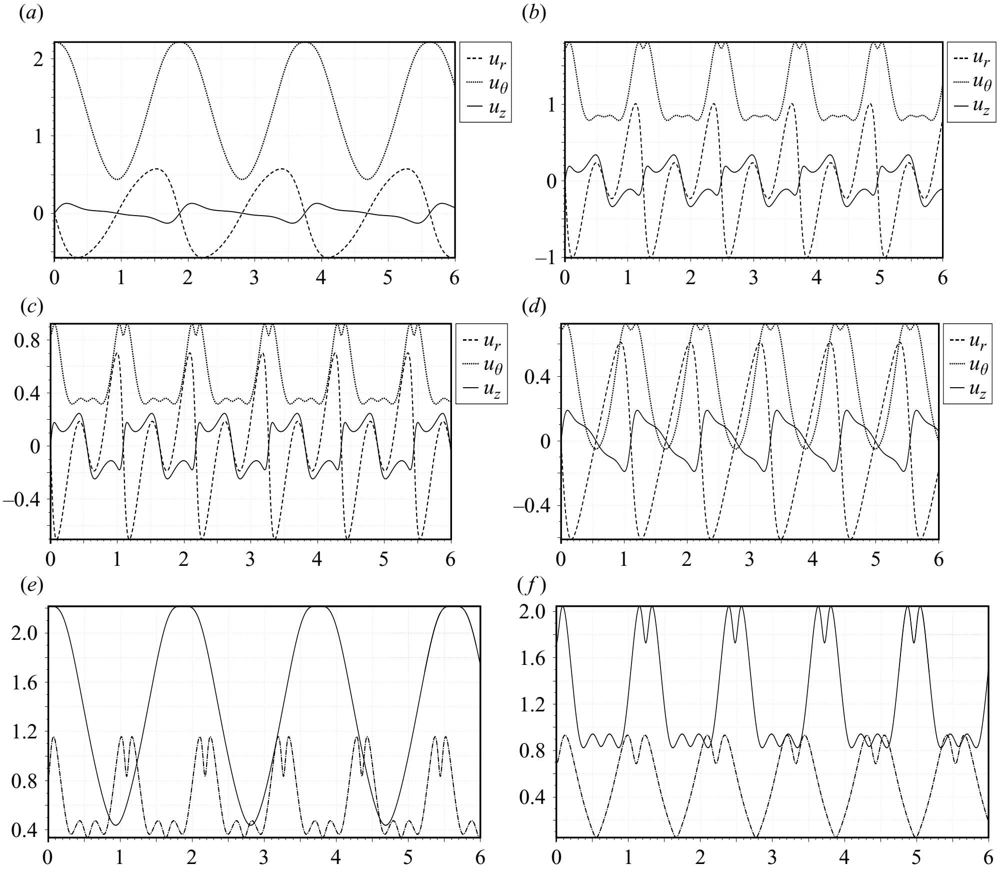

FIGURE 17. Cylindrical velocity components (*a–d*) and the associated speed (*e*, *f*) as a function of time (measured in spheroid revolutions) evaluated along the trajectory determined by the initial condition $\boldsymbol{x}^*(0) = (1.25\ \text{CR}, 0, 0.5\ \text{CH})$ for eccentricity $e = 0.95$ (*a*, *b*) and $e = 0.995$ (*c*, *d*). These are the central trajectories in figures 2(*a–d*) and 3(*a–d*). Each feature is provided for cone angles $\kappa = 30°$ (left-hand column) and $\kappa = 60°$ (right-hand column) over 6 spheroid revolutions. The eccentricity of the associated speeds in (*e*) and (*f*) are 0.95 (solid line) and 0.995 (broken line).

across figures 17(*e*) and 17(*f*). The structure in velocity and speed as the particle and spheroid continually meet and pass dictates the epicyclic nature of a particle trajectory.

6. Far-field behaviour

It is natural to ask how the velocity field decays as $|\boldsymbol{x}| \to \infty$. By expanding (3.14) in $1/|\boldsymbol{x}| \ll 1$, it is found that

$$\boldsymbol{u}(\boldsymbol{x}) = -\boldsymbol{U}(\boldsymbol{x}) + \frac{4c^3}{3}[\omega \sin\kappa(\alpha\ \boldsymbol{u}_{SS}(\boldsymbol{x};\boldsymbol{e}_x,\boldsymbol{e}_y) + \widetilde{\gamma}_1\ \boldsymbol{u}_R(\boldsymbol{x};\boldsymbol{e}_z)) + \widetilde{\gamma}_2(\omega\cos\kappa + \dot{\sigma})\ \boldsymbol{u}_R(\boldsymbol{x};\boldsymbol{e}_x)] + O\left(\frac{1}{|\boldsymbol{x}|^3}\right) \tag{6.1}$$

where $\dot{\sigma}$ is the rate of an added rotation about the spheroid's major axis as it sweeps out a cone. The exact velocity field induced by this additional rotation is discussed and constructed in the subsequent section. From the transformation in (3.7) which describes the velocity field in the laboratory frame, we obtain

$$\begin{aligned} \boldsymbol{u}^*(\boldsymbol{x}^*) = {} & \frac{4c^3}{3} \; R_\vartheta R_\kappa \left[\omega \sin\kappa \left(\alpha \; \boldsymbol{u}_{SS}\left(R_\kappa^T R_\vartheta^T \boldsymbol{x}^*; \boldsymbol{e}_x, \boldsymbol{e}_y\right) + \widetilde{\gamma}_1 \; \boldsymbol{u}_R\left(R_\kappa^T R_\vartheta^T \boldsymbol{x}^*; \boldsymbol{e}_z\right)\right)\right. \\ & \left. + \widetilde{\gamma}_2(\omega\cos\kappa + \dot{\sigma}) \; \boldsymbol{u}_R\left(R_\kappa^T R_\vartheta^T \boldsymbol{x}^*; \boldsymbol{e}_x\right)\right] \; + \; O\left(\frac{1}{|\boldsymbol{x}^*|^3}\right) \\ = {} & \frac{4c^3}{3}(\alpha \; \omega \;\; \sin\kappa \;\; \boldsymbol{u}_{SS}(\boldsymbol{x}^*; \boldsymbol{e}_x^*(t), \boldsymbol{e}_y^*(t)) + \widetilde{\gamma}_1 \; \omega \;\; \cos\kappa \;\; \boldsymbol{u}_R(\boldsymbol{x}^*; \boldsymbol{e}_z^*(t)) \\ & + \widetilde{\gamma}_2 \; (\omega\cos\kappa + \dot{\sigma}) \; \boldsymbol{u}_R(\boldsymbol{x}^*; \boldsymbol{e}_x^*(t))), \end{aligned} \tag{6.2}$$

at leading order.

Recall that the transformation $\boldsymbol{x}^*(t) = R_\vartheta R_\kappa \boldsymbol{x}$ moves from a fixed reference frame defined in $\boldsymbol{x}$ where the spheroid is lying on the x-axis embedded in a flow to the laboratory frame defined in $\boldsymbol{x}^*$ where the spheroid is tilted sweeping out a cone in a fluid otherwise at rest. If $\boldsymbol{e}_x, \boldsymbol{e}_y, \boldsymbol{e}_z$ represent the basis vectors in the $\boldsymbol{x}$-coordinate system then the columns of $R_\vartheta R_\kappa$ represent the basis vectors in the $\boldsymbol{x}^*$-coordinate system. Hence, the singularity strengths in (6.2) are

$$\left.\begin{aligned} \boldsymbol{e}_x^*(t) = R_\vartheta R_\kappa \boldsymbol{e}_x = \begin{pmatrix} \sin\kappa\cos\vartheta(t) \\ \sin\kappa\sin\vartheta(t) \\ \cos\kappa \end{pmatrix}, \quad \boldsymbol{e}_y^*(t) = R_\vartheta R_\kappa \boldsymbol{e}_y = \begin{pmatrix} -\sin\vartheta(t) \\ \cos\vartheta(t) \\ 0 \end{pmatrix}, \\ \boldsymbol{e}_z^*(t) = R_\vartheta R_\kappa \boldsymbol{e}_y = \begin{pmatrix} -\cos\kappa\cos\vartheta(t) \\ -\cos\kappa\sin\vartheta(t) \\ \sin\kappa \end{pmatrix}, \end{aligned}\right\} \tag{6.3}$$

providing $\boldsymbol{e}_x^*(t)$ is aligned along the spheroid in the $\boldsymbol{x}^*$ system while $\boldsymbol{e}_y^*(t)$ and $\boldsymbol{e}_z^*(t)$ replace $\boldsymbol{e}_y$ and $\boldsymbol{e}_z$, respectively. The time-dependence in the system of ordinary differential equations governing the far-field motion (6.2) enters through the strengths of the singularities.

In its entirety, at leading order, fluid particle trajectories $\boldsymbol{x}^*(t) = (x^*(t), y^*(t), z^*(t))$ in the far field are found by imposing the initial condition

$$\boldsymbol{x}^*(0) = \boldsymbol{x}_0^* \tag{6.4}$$

and solving the non-autonomous system

$$\begin{aligned} \frac{\mathrm{d}x^*}{\mathrm{d}t} = \frac{4c^3}{3} & \left(\frac{\widetilde{\gamma}_1\omega\sin\kappa(-y^*\sin\kappa - z^*\sin\vartheta(t)\cos\kappa)}{|\boldsymbol{x}^*|^3}\right. \\ & + \frac{\widetilde{\gamma}_2(\omega\cos\kappa + \dot{\sigma})(-y^*\cos\kappa + z^*\sin\vartheta(t)\sin\kappa))}{|\boldsymbol{x}^*|^3} \\ & \left.\times \frac{3\,\omega\alpha\sin\kappa(-x^*\sin\vartheta(t) + y^*\cos\vartheta(t))(\sin\kappa(x^*\cos\vartheta(t) + y^*\sin\vartheta(t)) + z^*\cos\kappa)x^*}{|\boldsymbol{x}^*|^5}\right) \\ \frac{\mathrm{d}y^*}{\mathrm{d}t} = \frac{4c^3}{3} & \left(\frac{\widetilde{\gamma}_1\omega\sin\kappa(x^*\sin\kappa + z^*\cos\vartheta(t)\cos\kappa)}{|\boldsymbol{x}^*|^3}\right. \\ & + \frac{\widetilde{\gamma}_2(\omega\cos\kappa + \dot{\sigma})(x^*\cos\kappa - z^*\cos\vartheta(t)\sin\kappa))}{|\boldsymbol{x}^*|^3} \\ & \left.\times \frac{3\,\omega\alpha\sin\kappa(-x^*\sin\vartheta(t) + y^*\cos\vartheta(t))(\sin\kappa(x^*\cos\vartheta(t) + y^*\sin\vartheta(t)) + z^*\cos\kappa)y^*}{|\boldsymbol{x}^*|^5}\right) \end{aligned}$$

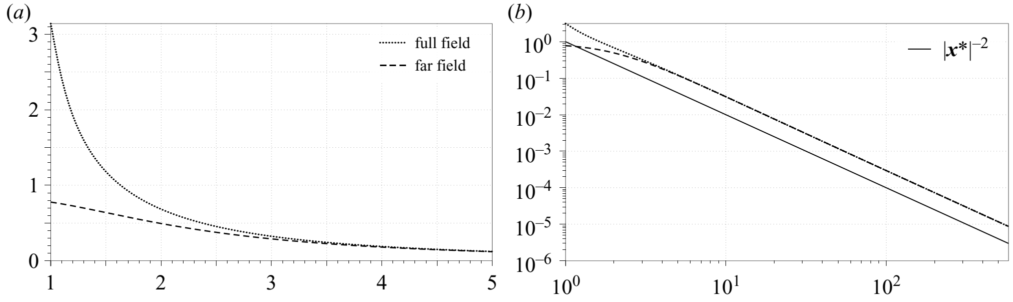

FIGURE 18. Speed as a function of x^* for the exact velocity field when cone angle $\kappa = 30°$, eccentricity $e = 0.95$, $y^* = 0$, and $z^* = \text{CH}$ compared to the speed of the far-field velocity field in (6.2). (*a*) Comparison near the cone structure; (*b*) log–log plot of speed for larger x^*. The log–log plot demonstrates the $|\boldsymbol{x}^*|^{-2}$ scaling behaviour.

$$\frac{\mathrm{d}z^*}{\mathrm{d}t} = \frac{4c^3}{3}\left(\frac{\widetilde{\gamma_1}\omega \sin\kappa\cos\kappa(x^*\sin\vartheta(t) - y^*\cos\vartheta(t)}{|\boldsymbol{x}^*|^3}\right.$$
$$+\frac{\widetilde{\gamma_2}(\omega\cos\kappa + \dot{\sigma})\sin\kappa(-x^*\sin\vartheta(t) + y^*\cos\vartheta(t)))}{|\boldsymbol{x}^*|^3}$$
$$\left.\times\ \frac{3\,\omega\alpha\sin\kappa(-x^*\sin\vartheta(t) + y^*\cos\vartheta(t))(\sin\kappa(x^*\cos\vartheta(t) + y^*\sin\vartheta(t)) + z^*\cos\kappa)z^*}{|\boldsymbol{x}^*|^5}\right).$$

It is of interest to examine

$$\frac{1}{2}\frac{\mathrm{d}(|\boldsymbol{x}^*|^2)}{\mathrm{d}t} = \boldsymbol{x}^* \cdot \frac{\mathrm{d}\boldsymbol{x}^*}{\mathrm{d}t}. \tag{6.5}$$

By design, the rotlet singularity offers no contribution to $\boldsymbol{x}^* \cdot \mathrm{d}\boldsymbol{x}^*/\mathrm{d}t$. However, the stresslet singularity in (6.2) makes the rate of change of $|\boldsymbol{x}^*|^2$ in the far field

$$\frac{\mathrm{d}(|\boldsymbol{x}^*|^2)}{\mathrm{d}t} = \frac{8c^3\ \omega\ \alpha\sin\kappa\ (\boldsymbol{e}_y^* \cdot \boldsymbol{x}^*)(\boldsymbol{e}_z^* \cdot \boldsymbol{x}^*)}{3\ |\boldsymbol{x}^*|^3} \tag{6.6}$$

and non-zero at leading order.

6.1. *Trajectory property scaling*

The velocity field decays like $|\boldsymbol{x}^*|^{-2}$ in the far field as provided by singularities at leading order in (6.2). The magnitude of the three-dimensional velocity field is measured in the laboratory frame for $y^* = 0$ and $z^* = \text{CH}$ as x^* increases (figure 18). This figure shows speed for the exact solution and the far-field expansion near the cone structure in addition to a log–log plot of the ensuring speed for larger x^* as compared to a $|\boldsymbol{x}^*|^{-2}$ scaling.

The far-field system does not readily predict the scaling of trajectory properties analytically. Figure 19 provides a numerical sample of the scaling of polar amplitude, the angle travelled, vertical fluctuation, and arclength when the cone angle $\kappa = 30°$ and eccentricity $e = 0.95$. The properties in these figures are measured on trajectories after a single spheroid revolution for $y_0 = 0$ and $z_0 = \text{CH}$ as x^* increases. For arbitrary cone angle κ and spheroid eccentricity e, it can be numerically shown that for $|\boldsymbol{x}^*| \gg 1$,

$$\text{Polar amplitude} \sim |\boldsymbol{x}^*|^{-2}, \quad \text{Angle travelled} \sim |\boldsymbol{x}^*|^{-3}, \tag{6.7}$$

$$\text{Vertical fluctuation} \sim |\boldsymbol{x}^*|^{-2}, \quad \text{Arclength} \sim |\boldsymbol{x}^*|^{-2}. \tag{6.8}$$

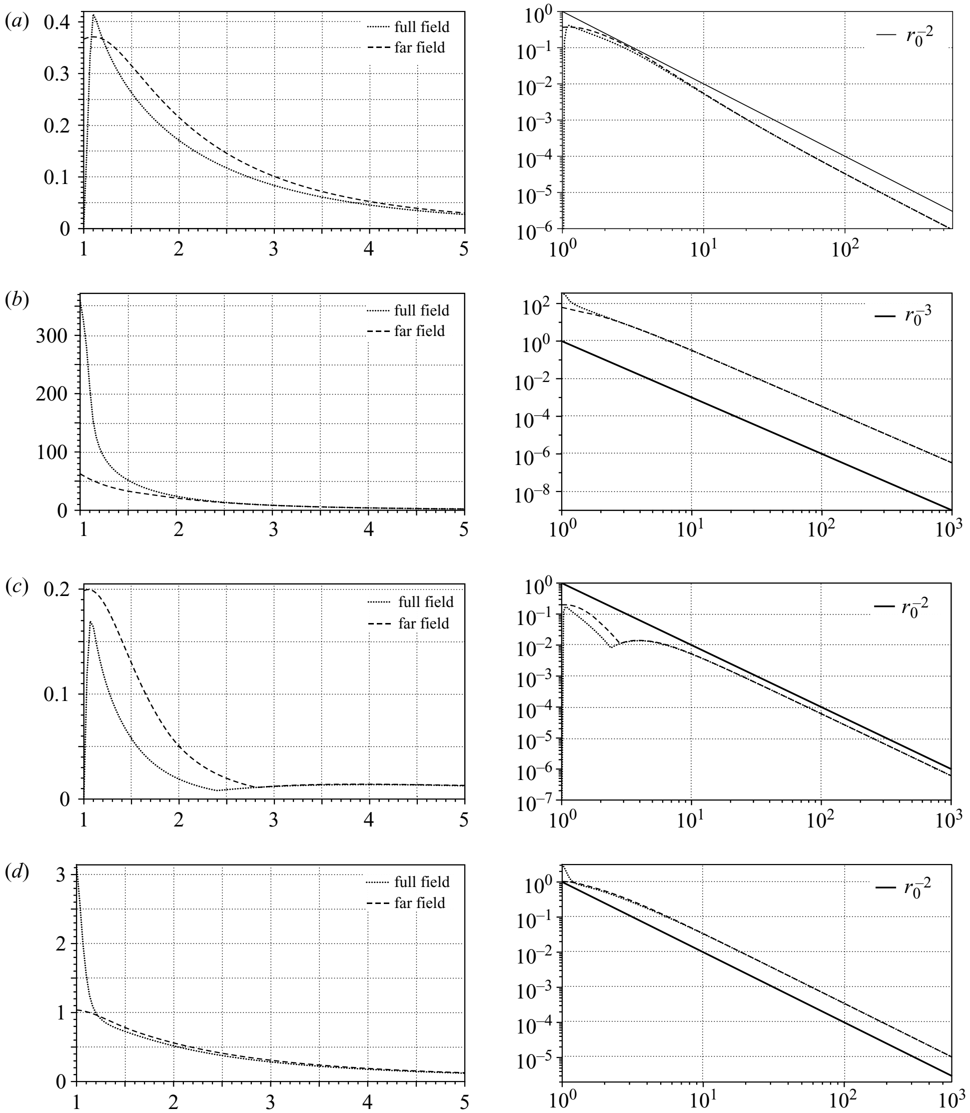

FIGURE 19. Trajectory properties as a function of initial cylindrical radius $r_0 = \sqrt{x_0^2 + y_0^2}$ for the exact velocity field when the cone angle $\kappa = 30°$, eccentricity $e = 0.95$, $y_0 = 0$, and $z_0 = \mathrm{CH}$ compared to those of the far-field velocity field in (6.2). The left-hand column shows the comparison near the cone structure while the right-hand column shows a log–log plot of these properties for larger r_0. The log–log plot includes the scaling behaviour of each property as a function of r_0. (*a*) Polar amplitude; (*b*) angle travelled; (*c*) vertical fluctuation; (*d*) arclength.

The $|\boldsymbol{x}^*|^{-3}$ decay of angle travelled is consistent with the $|\boldsymbol{x}^*|^{-2}$ decay of arclength by definition of arclength as radius multiplied by angle.

6.2. *Far-field small cone angle κ limit*

Consider an expansion of the far-field velocity field in the laboratory frame in (6.2) for small cone angle κ. Retaining only $O(\kappa)$ terms yields

$$
\begin{aligned}
\frac{\mathrm{d}\boldsymbol{x}^*}{\mathrm{d}t} &= v_0(\boldsymbol{x}^*) + \kappa\, v_1(\boldsymbol{x}^*, t) \\
&= \frac{4c^3\widetilde{\gamma}_2\,\omega}{3|\boldsymbol{x}^*|^3}\begin{pmatrix} -y^* \\ x^* \\ 0 \end{pmatrix} + \kappa\left[\frac{4c^3(\widetilde{\gamma}_2-\widetilde{\gamma}_1)\,\omega}{3|\boldsymbol{x}^*|^3}\begin{pmatrix} z^*\sin\vartheta(t) \\ -z^*\cos\vartheta(t) \\ -x^*\sin\vartheta(t)+y^*\cos\vartheta(t) \end{pmatrix}\right. \\
&\quad \left. + \frac{4c^3\alpha\,\omega}{|\boldsymbol{x}^*|^5}(-x^*\sin\vartheta(t)+y^*\cos\vartheta(t))\,z^*\begin{pmatrix} x^* \\ y^* \\ z^* \end{pmatrix}\right]
\end{aligned}
\tag{6.9}
$$

for $|\boldsymbol{x}| \gg 1$. At leading order, the far-field velocity field is a single rotlet oriented in the positive z^*-direction, as might be expected. Transforming to spherical polar coordinates,

$$
x^* = r\cos\theta\sin\phi, \quad y^* = r\sin\theta\sin\phi, \quad z^* = r\cos\phi, \tag{6.10}
$$

with $0 \leqslant \phi < \pi$ and $0 \leqslant \theta < 2\pi$, the system in (6.9) is rewritten as

$$
\left.
\begin{aligned}
\frac{\mathrm{d}r}{\mathrm{d}t} &= \kappa\,\frac{2c^3\alpha\,\omega}{r^2}\,\sin 2\phi\,\sin(\theta-\vartheta(t)), \\
\frac{\mathrm{d}\phi}{\mathrm{d}t} &= \kappa\,\frac{4c^3(\widetilde{\gamma}_1-\widetilde{\gamma}_2)\,\omega}{3r^2}\,\sin(\theta-\vartheta(t)), \\
\frac{\mathrm{d}\theta}{\mathrm{d}t} &= \frac{4c^3\widetilde{\gamma}_2\,\omega}{3r^2}\,\sin\phi + \kappa\,\frac{4c^3(\widetilde{\gamma}_1-\widetilde{\gamma}_2)\,\omega}{3r^2}\,\cos\phi\,\cos(\theta-\vartheta(t)).
\end{aligned}
\right\}
\tag{6.11}
$$

Notice that the body frame of reference described in (4.9) is obtained through the transformation $\varphi = \theta - \vartheta(t)$ which is readily available in (6.11). In this reference frame, the averaging theorem (Sanders & Verhulst 1985) can be invoked to show that r and ϕ stay within $O(\kappa)$ of their initial values for (long) times of order $O(1/\kappa)$. Notice further that an invariant

$$
r = \rho(\phi) \tag{6.12}
$$

exists for this system. In fact,

$$
\frac{\mathrm{d}r}{\mathrm{d}t} = \frac{\mathrm{d}\rho}{\mathrm{d}\phi}\,\frac{\mathrm{d}\phi}{\mathrm{d}t}, \tag{6.13}
$$

and by inspection

$$
\frac{\mathrm{d}\rho}{\mathrm{d}\phi} = \frac{3\alpha}{2(\widetilde{\gamma}_1-\widetilde{\gamma}_2)}\sin 2\phi, \tag{6.14}
$$

so that

$$
r = \rho(\phi) = \frac{3\alpha}{4(\widetilde{\gamma}_2-\widetilde{\gamma}_1)}\cos 2\phi + C. \tag{6.15}
$$

Rotational symmetry with respect to φ generates a surface when the constant of integration C is picked by the initial conditions r_0 and ϕ_0.

The invariant surface provides a reduction of the system by elimination of, say, ϕ through

$$
\cos 2\phi = \frac{4(\widetilde{\gamma}_2-\widetilde{\gamma}_1)}{3\alpha}\,(r-C). \tag{6.16}
$$

Away from initial conditions within a neighbourhood of order κ around $\phi_0 = 0, \pi/2$, the sign of $\sin 2\phi$ is fixed and thus, for $\vartheta(t) = \omega t$, the far-field small cone angle reduces to the (r, φ) system

$$\frac{\mathrm{d}r}{\mathrm{d}t} = \kappa\,\omega\,\frac{2c^3\alpha}{r^2}\,\mathscr{S}(r)\,\mathscr{C}(r)\,\sin\varphi, \tag{6.17a}$$

$$\frac{\mathrm{d}\varphi}{\mathrm{d}t} = \omega\left(-1 + \frac{4c^3\widetilde{\gamma}_2}{3r^2}\,\mathscr{S}(r) + \kappa\frac{4c^3(\widetilde{\gamma}_2 - \widetilde{\gamma}_1)}{3r^2}\,\mathscr{C}(r)\cos\varphi\right), \tag{6.17b}$$

with the notation

$$\mathscr{S}(r) \equiv \sqrt{\frac{1}{2}\left(1 - \frac{4(\widetilde{\gamma}_2 - \widetilde{\gamma}_1)}{3\alpha}(r - C)\right)}, \qquad \mathscr{C}(r) \equiv \sqrt{\frac{1}{2}\left(1 + \alpha\frac{4(\widetilde{\gamma}_2 - \widetilde{\gamma}_1)}{3\alpha}(r - C)\right)}.$$

This system can be reduced by quadratures with an appropriate integrating factor. The function

$$K = \int^r \left(\frac{-3s^2 + 4c^3\widetilde{\gamma}_2\,\mathscr{S}(s)}{6c^3\alpha\,\mathscr{S}(s)\,\mathscr{C}(s)}\exp\left(\int^s \frac{2(\widetilde{\gamma}_2 - \widetilde{\gamma}_1)}{3\,\alpha\,\mathscr{S}(u)}\mathrm{d}u\right)\right)\mathrm{d}s$$
$$+\kappa\cos\varphi\,\exp\left(\int^s \frac{2(\widetilde{\gamma}_2 - \widetilde{\gamma}_1)}{3\,\alpha\,\mathscr{S}(s)}\,\mathrm{d}s\right)$$

is invariant along solutions of system (6.18). This invariant evaluated at $\varphi = 0, \pi$ (where $\mathrm{d}r/\mathrm{d}\varphi = 0$ according to system (6.18)) yields an approximate expression for the (projected) epicycle amplitude as a function of the initial conditions r_0 and ϕ_0,

$$a_e \simeq \kappa\,\frac{12c^3\alpha\,(\mathscr{S}(r_0))^2\mathscr{C}(r_0)}{3r_0^2 - 4c^3\widetilde{\gamma}_2\,\mathscr{S}(r_0)}, \tag{6.18}$$

which shows explicitly the far field decay as $1/r_0^2$ by retaining the leading order of this expression for large r_0.

6.3. *Far-field cylindrical radial limit*

The limit of the exact velocity field as the cylindrical radius $\sqrt{x^{*2} + y^{*2}} \to \infty$ in the laboratory frame provides

$$\frac{\mathrm{d}x^*}{\mathrm{d}t} = \frac{4\omega c^3}{3}\left(\frac{3\,\alpha\sin^2\kappa\,(x^*\cos\vartheta + y^*\sin\vartheta)^2(-x^*\sin\vartheta + y * \cos\vartheta)}{(x^{*2} + y^{*2})^{5/2}} - \frac{y^*\,(\widetilde{\gamma}_1\,\sin^2\kappa + \widetilde{\gamma}_2\,\cos^2\kappa)}{(x^{*2} + y^{*2})^{3/2}}\right),$$

$$\frac{\mathrm{d}y^*}{\mathrm{d}t} = \frac{4\omega c^3}{3}\left(\frac{3\,\alpha\sin^2\kappa\,(x^*\cos\vartheta + y^*\sin\vartheta)(-x^*\sin\vartheta + y * \cos\vartheta)^2}{(x^{*2} + y^{*2})^{5/2}} + \frac{x^*\,(\widetilde{\gamma}_1\sin^2\kappa + \widetilde{\gamma}_2\cos^2\kappa)}{(x^{*2} + y^{*2})^{3/2}}\right),$$

$$\frac{\mathrm{d}z^*}{\mathrm{d}t} = \frac{4\omega c^3}{3}\left(\frac{(\widetilde{\gamma}_1 - \widetilde{\gamma}_2)\,\sin\kappa\,\cos\kappa\,(x^*\sin\vartheta - y^*\cos\vartheta)}{(x^{*2} + y^{*2})^{3/2}}\right).$$

Transforming to cylindrical coordinates

$$x^* = r\cos\theta, \quad y^* = r\sin\theta, \quad z^* = z,$$

this system is rewritten as

$$\frac{\mathrm{d}r}{\mathrm{d}t} = 2\,\omega\,c^3\,\alpha\sin^2\kappa\;\frac{\sin 2\varphi}{r^2}, \tag{6.19}$$

$$\frac{\mathrm{d}\varphi}{\mathrm{d}t} = \frac{4\omega c^3}{3}\left(-1+\frac{\widetilde{\gamma}_1\;\sin^2\kappa+\widetilde{\gamma}_2\;\cos^2\kappa}{r^2}\right), \tag{6.20}$$

$$\frac{\mathrm{d}z}{\mathrm{d}t} = \frac{2\,\omega\,c^3}{3}(\widetilde{\gamma}_1-\widetilde{\gamma}_2)\;\sin\kappa\;\cos\kappa\;\frac{\sin\varphi}{r^2}, \tag{6.21}$$

through the change of variables $\varphi=\theta-\vartheta(t)$. Notice the invariant $r=r(\varphi)$ where by inspection

$$\frac{\mathrm{d}r}{\mathrm{d}\varphi} = \frac{3\alpha\;\sin^2\kappa\;\sin 2\varphi}{2(-r^2+\widetilde{\gamma}_1\sin^2\kappa+\widetilde{\gamma}_2\cos^2\kappa)}. \tag{6.22}$$

This separable ordinary differential equation provides the invariant

$$\frac{2r^3}{3} - 2r\;(\widetilde{\gamma}_1\sin^2\kappa+\widetilde{\gamma}_2\cos^2\kappa) = \frac{3\,\alpha\;\sin^2\kappa\cos 2\varphi}{2}+C. \tag{6.23}$$

By using the fact that for sufficiently large r the left-hand side of (6.23) is monotonic increasing, the maximal excursion that the cylindrical radius can experience during the evolution governed by system (6.19)–(6.21) is determined by the maximal variation in φ of the right-hand side. Thus, for large initial radial conditions r_0, by a simple application of the mean value theorem, the projected epicycle amplitude is approximately

$$a_e \simeq \frac{3\,\alpha\;\sin^2\kappa}{2r_0^2}. \tag{6.24}$$

7. An additional rotation

We have examined the motion of a body sweeping out a cone defined by the boundary conditions in (3.9). This motion has a ‘dark side of the moon’ feature for which the surface of the spheroid interior to the cone swept by its long axis always remains on the interior. This constraint can be removed by considering an additional rotation about the major axis as it sweeps out a cone. It turns out that practical experimental set-ups, for which the present free precessing spheroid is an idealization, can induce this extra rotation owing to a combination of external forces (such as friction from the suspension point) and it is relevant to include its effects. This additional rotation can be imposed in the body frame of reference, and the velocity field in the laboratory frame can be constructed with the transformations of § 3.1.

Recall the boundary conditions for the auxiliary problem defined by (3.5). The far-field condition can be expressed as

$$R_\kappa^T\boldsymbol{U}(R_\kappa\boldsymbol{x}) = -\omega\sin\kappa(\boldsymbol{e}_z\times\boldsymbol{x})-\omega\cos\kappa(\boldsymbol{e}_x\times\boldsymbol{x}) \tag{7.1}$$

so that the velocity fields

$$\boldsymbol{v}^1(\boldsymbol{x}) = -\omega\sin\kappa\bigg((\boldsymbol{e}_z\times\boldsymbol{x}) - \int_{-c}^{c}(c^2-s^2)[\alpha\boldsymbol{u}_{SS}(\boldsymbol{x}-\boldsymbol{s};\boldsymbol{e}_x,\boldsymbol{e}_y)+\widetilde{\gamma}_1\boldsymbol{u}_R(\boldsymbol{x}-\boldsymbol{s};\boldsymbol{e}_z)]\,\mathrm{d}s$$
$$+\beta\int_{-c}^{c}(c^2-s^2)^2\frac{\partial}{\partial y}\boldsymbol{u}_D(\boldsymbol{x}-\boldsymbol{s};\boldsymbol{e}_x)\,\mathrm{d}s\bigg), \tag{7.2a}$$

$$\boldsymbol{v}^2(\boldsymbol{x}) = -\omega\cos\kappa\left((\boldsymbol{e}_x\times\boldsymbol{x}) - \widetilde{\gamma}_2\int_{-c}^{c}(c^2-s^2)\boldsymbol{u}_R(\boldsymbol{x}-\boldsymbol{s},\boldsymbol{e}_x)\,\mathrm{d}s\right), \tag{7.2b}$$

satisfy Stokes equations with boundary conditions

$$\left.\begin{aligned} &\boldsymbol{v}^1(\boldsymbol{x}_0) = 0,\\ &\lim_{\boldsymbol{x}\to\infty}\boldsymbol{v}^1(\boldsymbol{x}) = -\omega\sin\kappa(\boldsymbol{e}_z\times\boldsymbol{x}),\end{aligned}\right\} \tag{7.3a}$$

$$\left.\begin{aligned} &\boldsymbol{v}^2(\boldsymbol{x}_0) = 0,\\ &\lim_{\boldsymbol{x}\to\infty}\boldsymbol{v}^2(\boldsymbol{x}) = -\omega\cos\kappa(\boldsymbol{e}_x\times\boldsymbol{x}),\end{aligned}\right\} \tag{7.3b}$$

where $\boldsymbol{x}_0$ lies on the boundary of the spheroid in the body frame of reference given in (3.1).

Consider an additional rotation of rate $\dot{\sigma}$ on the spheroid about its major axis. The resulting laboratory-frame motion is constructed through a transformation of the solution to the auxiliary boundary-value problem

$$\left.\begin{aligned} &\boldsymbol{v}(\boldsymbol{x}_0) = \boldsymbol{V}(\boldsymbol{x}_0),\\ &= \dot{\sigma}(\boldsymbol{e}_x\times\boldsymbol{x}_0),\\ &\lim_{\boldsymbol{x}\to\infty}\boldsymbol{v}(\boldsymbol{x}) = R_\kappa^T\boldsymbol{U}(R_\kappa\boldsymbol{x}).\end{aligned}\right\} \tag{7.4}$$

The solution to Stokes equations which satisfies

$$\left.\begin{aligned} &\boldsymbol{u}(\boldsymbol{x}_0) = 0,\\ &\lim_{\boldsymbol{x}\to\infty}\boldsymbol{u}(\boldsymbol{x}) = R_\kappa^T\boldsymbol{U}(R_\kappa\boldsymbol{x}),\end{aligned}\right\} \tag{7.5}$$

has been determined in (3.14). By examining the velocity field $\boldsymbol{v}_2$ in (7.2*b*) and (7.3*b*), it is clear that

$$\widetilde{\boldsymbol{v}}(\boldsymbol{x}) = \dot{\sigma}\;\widetilde{\gamma}_2\int_{-c}^{c}(c^2-s^2)\boldsymbol{u}_R(\boldsymbol{x}-\boldsymbol{s},\boldsymbol{e}_x)\,\mathrm{d}s \tag{7.6}$$

satisfies

$$\left.\begin{aligned} &\widetilde{\boldsymbol{v}}(\boldsymbol{x}_0) = \dot{\sigma}(\boldsymbol{e}_x\times\boldsymbol{x}_0),\\ &\lim_{\boldsymbol{x}\to\infty}\widetilde{\boldsymbol{v}}(\boldsymbol{x}) = 0,\end{aligned}\right\} \tag{7.7}$$

and, accordingly,

$$\begin{aligned} \boldsymbol{v}(\boldsymbol{x}) &= \widetilde{\boldsymbol{v}}(\boldsymbol{x}) + \boldsymbol{u}(\boldsymbol{x})\\ &= -\omega\sin\kappa(\boldsymbol{e}_z\times\boldsymbol{x}) - \omega\sin\kappa(\boldsymbol{e}_x\times\boldsymbol{x})\\ &\quad+\omega\sin\kappa\int_{-c}^{c}(c^2-s^2)[\alpha\boldsymbol{u}_{SS}(\boldsymbol{x}-\boldsymbol{s};\boldsymbol{e}_x,\boldsymbol{e}_y)+\widetilde{\gamma}_1\boldsymbol{u}_R(\boldsymbol{x}-\boldsymbol{s};\boldsymbol{e}_z)]\,\mathrm{d}s\\ &\quad+\omega\beta\cos\kappa\int_{-c}^{c}(c^2-s^2)^2\frac{\partial}{\partial y}\boldsymbol{u}_D(\boldsymbol{x}-\boldsymbol{s};\boldsymbol{e}_x)\,\mathrm{d}s\\ &\quad+(\omega\cos\kappa+\dot{\sigma})\widetilde{\gamma}_2\int_{-c}^{c}(c^2-s^2)\boldsymbol{u}_R(\boldsymbol{x}-\boldsymbol{s},\boldsymbol{e}_x)\,\mathrm{d}s \end{aligned} \tag{7.8}$$

is determined as the appropriate body-frame velocity field.

Reconsider the transformations R_κ and R_ϑ in § 3.1, which tilted the spheroid and made the body rotate around the vertical axis to sweep out a cone. Applying these transformations in the same manner, results in the laboratory frame velocity field

$$\boldsymbol{v}^*(x^*) = -\boldsymbol{U}(\boldsymbol{x}^*) + R_\vartheta R_\kappa \boldsymbol{v}\left(R_\kappa^T R_\vartheta^T \boldsymbol{x}^*\right) \tag{7.9}$$

whose boundary conditions are

$$\left.\begin{aligned} \boldsymbol{v}^*(\boldsymbol{x}_0^*) &= -\boldsymbol{U}(\boldsymbol{x}_0^*) + \boldsymbol{V}^*(\boldsymbol{x}_0^*), \\ \lim_{\boldsymbol{x}^*\to\infty} \boldsymbol{v}^*(\boldsymbol{x}^*) &= \boldsymbol{0}, \end{aligned}\right\} \tag{7.10}$$

where $\boldsymbol{U}(\boldsymbol{x}) = \omega\,(y, -x, 0)$, as before, and

$$\begin{aligned} \boldsymbol{V}^*(\boldsymbol{x}^*) &= R_\vartheta R_\kappa \boldsymbol{V}\left(R_\kappa^T R_\vartheta^T \boldsymbol{x}^*\right) \\ &= \dot\sigma \begin{pmatrix} -y^* \cos\kappa + z^* \sin\kappa \sin\vartheta(t) \\ x^* \cos\kappa - z^* \sin\kappa \cos\vartheta(t) \\ \sin\kappa(-x^* \sin\vartheta(t) + y^* \cos\vartheta(t)) \end{pmatrix}. \end{aligned} \tag{7.11}$$

A discussion of Euler angles and general rigid-body motions in Appendix E shows that the boundary-value problem in (7.4) is the correct one to consider, before a transformation to the laboratory frame is applied, to model an added rotation of the spheroid about its major axis as it sweeps out a cone.

A comparison between trajectories with and without this additional axial rotation is given in figures 20 and 21 for cone angle $\kappa = 45°$ and eccentricity $e = 0.95$. These figures also show the corresponding trajectories in the generator body frame found through the transformation in (4.8). The boundary conditions in this body reference frame are

$$\left.\begin{aligned} \boldsymbol{v}'(\boldsymbol{x}_0') &= \dot\sigma R_\kappa \left(\boldsymbol{e}_x \times R_\kappa^T \boldsymbol{x}_0'\right) \\ &= \dot\sigma (R_\kappa \boldsymbol{e}_x \times \boldsymbol{x}_0'), \\ \lim_{\boldsymbol{x}\to\infty} \boldsymbol{v}'(\boldsymbol{x}') &= \boldsymbol{U}(\boldsymbol{x}') \\ &= -\omega(\boldsymbol{e}_x \times \boldsymbol{x}') \end{aligned}\right\} \tag{7.12}$$

where the vector $R_\kappa \boldsymbol{e}_x = (\sin\kappa,\ 0,\ \cos\kappa)$ is aligned along the tilted spheroid's major axis. Consequently, the body frame of reference is that of a spheriod tilted in the (x', z')-plane by an angle κ, rotating about its major axis in the counterclockwise direction with rate $\dot\sigma$, while embedded in a clockwise rotation of the (x', y')-plane with rate ω. The closed orbits on the right-hand sides of figures 20 and 21 generate the laboratory-frame trajectories given on left.

In figure 7, a collection of body-frame orbits that climbed and wrapped the spheroid was presented. Initial positions dictated whether a fluid particle passed in front of the spheroid or routed around the body enclosing it. The intermediate motion was one for which a fluid particle climbed along the length of the spheroid to its tip. The analogous image for an added axial rotation is shown in figure 22. In particular, the transition between generator frame trajectories that enclose the spheroid, and those that do not, is illustrated. The body-frame orbits in figure 22 are determined from the same ten initial positions of figure 7, without the axial rotation. In that figure, small changes in initial position ($x_0 = -0.2349584$ to $x_0 = -0.2349587$) resulted in noticeably different trajectories as fluid particles climbed farther up the length of the spheroid. When an axial rotation rate is present, these trajectories in figure 22 are not as easily distinguished, although still present. Figure 22 demonstrates that the transition between bypassing or containing the spheroid is a body-frame generator

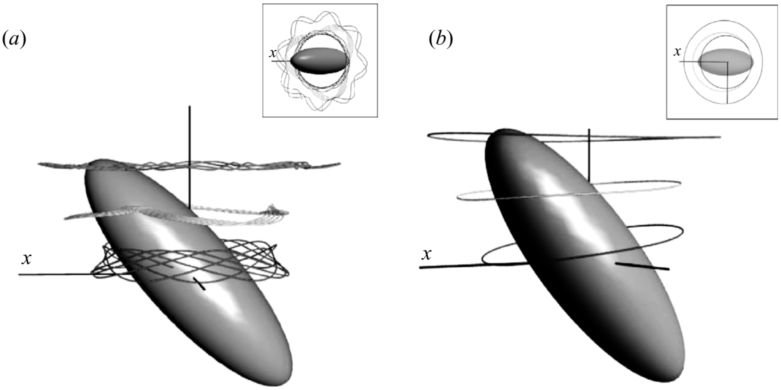

FIGURE 20. (*a*) Laboratory-frame trajectories and (*b*) the corresponding generators of a spheroid that experiences no secondary rotation about its major axis. The initial conditions are the same as those in figures 2 and 3 but with cone angle $\kappa = 45^\circ$ and eccentricity $e = 0.95$. These trajectories are a comparative reference for the trajectories in figure 21 which result from an additional axial rotation of the spheroid about its major axis. Insets show view from the top.

which nearly closes on itself before veering off and passing in front of the body. At this axial rotation rate, each sampled initial position produces a generator that bypasses the spheroid. As the axial rotation rate increases, however, generators begin to route around the body enclosing it as depicted in figure 23 for $\dot{\sigma} = 10\sqrt{5}\,\omega$. For large axial rotation rates $\dot{\sigma}$, the body-frame velocity field is dominated by the distribution of rotlets in (7.8) which are aligned along the spheroid's major axis. The rotlet velocity field results from a point source of torque applied to Stokes flow, accounting for the circular-like generators also observed in figure 21 (for $\dot{\sigma} = 100\sqrt{5}\,\omega$).

Figures 20 to 25 display a rich collection of laboratory frame trajectories with greatly varying properties. An enhanced vertical fluctuation is evident in the fluid particle motion induced by the secondary added axial rotation. Figure 25 shows greyscale density plots of polar amplitude and vertical fluctuation for cone angle $\kappa = 30^\circ$ and eccentricity $e = 0.95$ when the axial rotation rate is $\dot{\sigma} = 2\omega$. The density plots display the spatial structure of these trajectory properties as a function of initial position $(x_0, 0, z_0)$ as defined and discussed in § 4. The reflectional symmetry about the plane containing the z-axis (the direction of the precession angular velocity vector) and the body's axis is maintained with an added axial rotation, as evident from the lateral view depicted in figure 24. It is further observed that trajectory properties, over varying initial position, are similar in structure when the axial rotation rate is fixed. This is additionally apparent in figures 9 and 14 which depict polar amplitude and vertical fluctuation when there is no axial rotation of the spheroid.

Finally, we remark that the far-field asymptotic analysis of the previous section can be easily expanded to account for the additional axial rotation parameter, which modifies the singularity distribution by an extra rotlet contribution.

8. Conclusion and discussion

We have presented a detailed study of the exact low-Reynolds-number hydrodynamic motion induced by a prolate spheroid sweeping a symmetric double cone, with and without secondary body spin. This fluid flow exhibits strong three dimensionality, spheroid geometry dependence, and Lagrangian trajectories characterized by orbits and epicycles. Typically, outside the cone structure, these

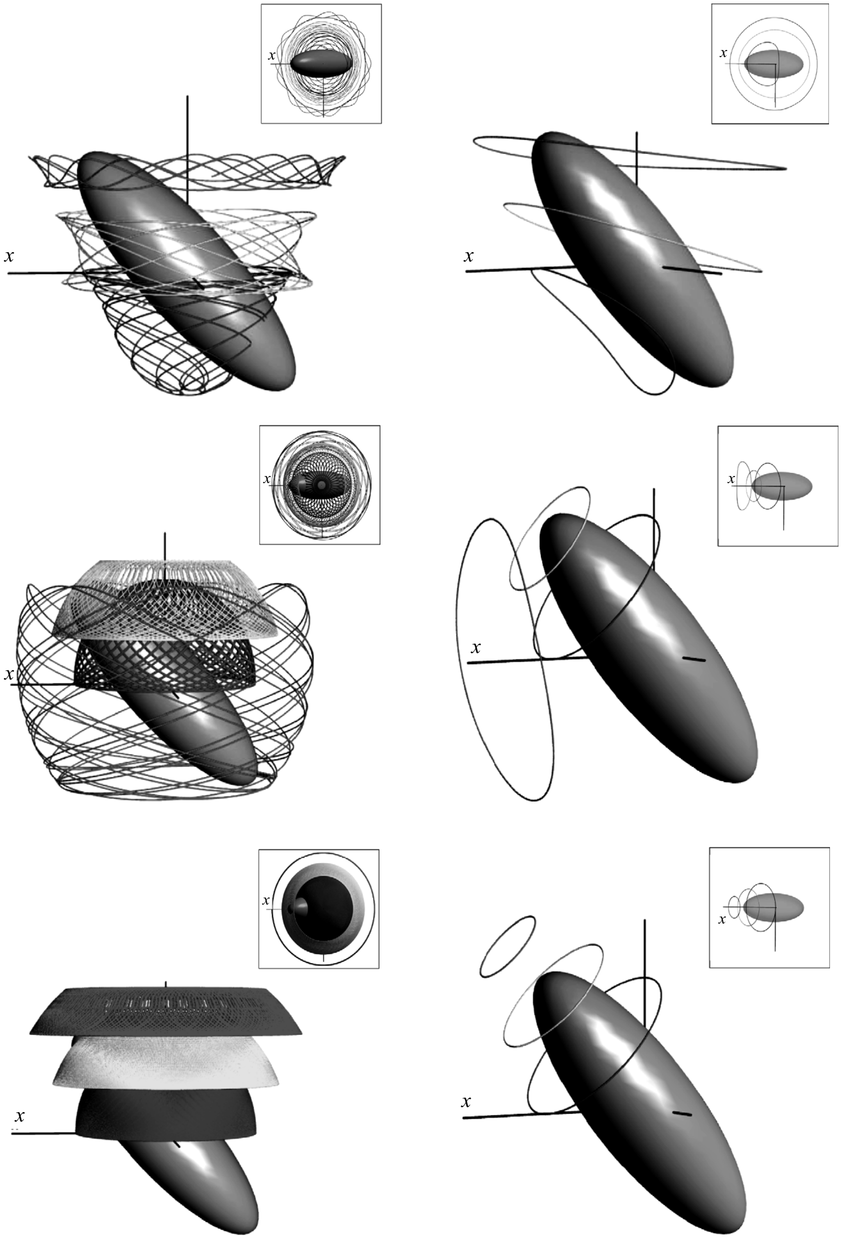

FIGURE 21. Laboratory-frame trajectories (left) resulting from a spheroid which rotates about its major axis as it sweeps out a cone and the corresponding generators (right) in the body frame of reference described by (7.12). The trajectories are shown for cone angle $\kappa = 45^\circ$ and eccentricity $e = 0.95$ with axial rotation rates $\dot{\sigma} = \sqrt{5}\,\omega,\ 10\sqrt{5}\,\omega,\ 100\sqrt{5}\,\omega$ (top to bottom) where $\omega = 2\pi$ is the rotation rate of sweeping out a cone. The initial conditions are the same as those in figures 2 and 3. Insets show top views, with body rendered translucently for panels on the right-hand side in order to show entire generator orbits.

orbits are characterized by slow orbits, and fast epicycles roughly commensurate with the rod rotation rate, while inside and near the cone structure, the behaviour is more complicated. By appealing to a generator written in the body-frame coordinates, the motion can be recognized as autonomous, and in all cases studied, the orbits

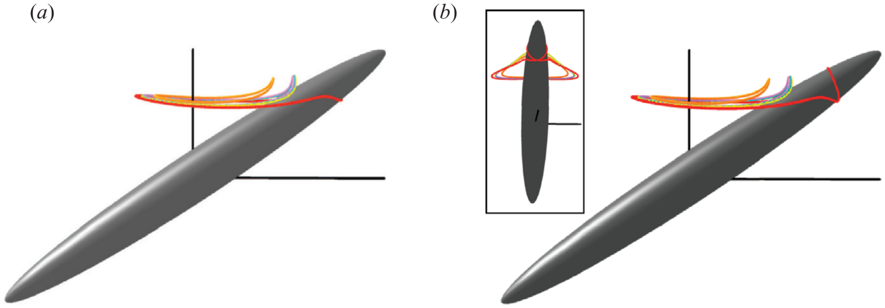

FIGURE 22. Body-frame orbits from an axial rotation of a spheroid with rate $\dot{\sigma} = 0.078491\sqrt{5}\,\omega$ (a) and rate $\dot{\sigma} = 0.078492\sqrt{5}\,\omega$ (b) where $\omega = 2\pi$ is the rate of the background rotation. The cone angle $\kappa = 60°$, eccentricity $e = 0.995$, and initial positions (x_0 CR, 0, 0.65 CH) are the same as those in figure 7 in which the spheroid does not rotate about its major axis. The values of x_0 are provided in the key of figure 8 and vary between -0.3 CR and -0.2 CR. As the axial rotation rate increases, the red periodic orbit (generator) transitions from enclosing the spheroid in (b) to passing in front of it. The inset figure shows that the generator, in its flyby in front of the spheroid, is close to a self-intersecting topological figure of eight curve, indicating the possibility of existence of a pair of homoclinic connections encircling the body and emanating from a fixed point at the intersection.

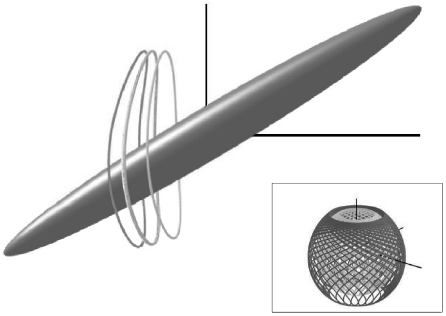

FIGURE 23. Body-frame orbits from an axial rotation of a spheroid with rate $\dot{\sigma} = 10\sqrt{5}\,\omega$ where $\omega = 2\pi$ is the rate of the background rotation. The cone angle $\kappa = 60°$, eccentricity $e = 0.995$, and initial positions (x_0 CR, 0, 0.65 CH) are the same as those in figure 7 and figure 22 in which the spheroid does not rotate about its major axis. In the inset, the corresponding laboratory-frame trajectories are shown for the left- and right-most generators. As $\dot{\sigma}$ increases, the velocity field is dominated by rotlet singularities directed along the spheroid's major axis.

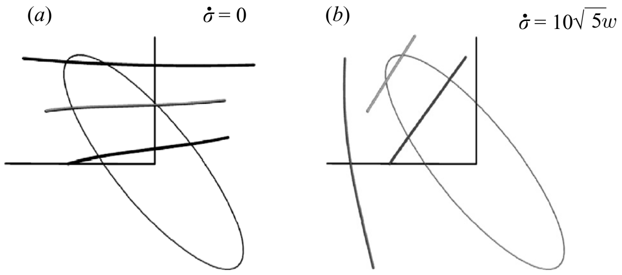

FIGURE 24. Lateral views (projection on the (x, z)-plane) of periodic orbits of rate $\dot{\sigma}$ generated by the same initial conditions as in figure 20 with (b) or without (a) axial rotation. The projection brings forth the reflectional symmetry with respect to the (x, z)-plane of generic periodic fluid particle trajectories (the portions of the orbit above and below this plane project onto the same curve segment in the (x, z)-plane).

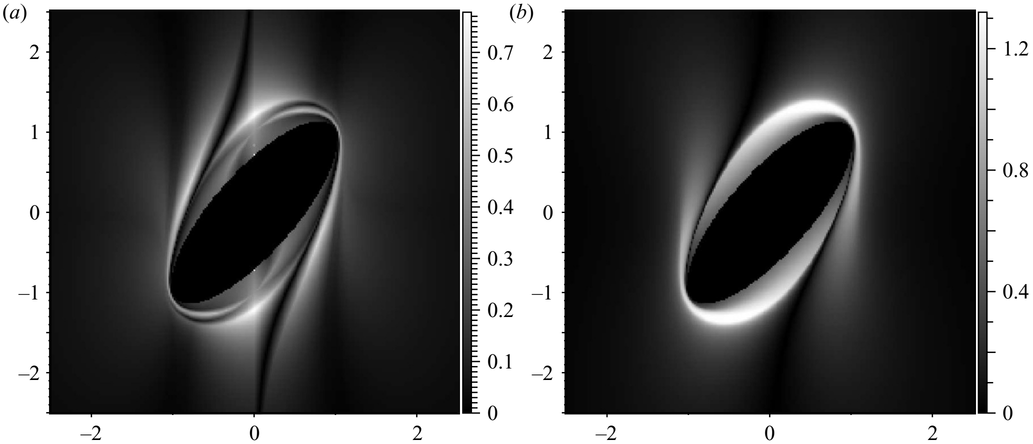

FIGURE 25. Greyscale density plots of polar amplitude (*a*) and vertical fluctuation (*b*) measured on trajectories from a spheroid that rotates about its major axis with rate $\dot{\sigma} = 2\omega$ while it sweeps out a cone at a rate $\omega = 2\pi$ once. The trajectories are initialized at the position $(x_0, 0, z_0)$. Greyscale is the trajectory property while the horizontal axis is x_0 (measured in cone radius CR) and the vertical axis is z_0 (measured in cone height CH).

close. Numerical results from integrating the particle motion induced by this exact mathematical solution show the possibility of a three-dimensional separatrix in the body-frame coordinate system. Detailed numerical studies present a spatial mapping of the behaviour of the Lagrangian trajectories as characterized by their epicycle size, angle travelled, vertical fluctuation and arclength. We have additionally found an invariant at far field and small cone angles which reduces the particle motion equations to a two-dimensional steady nonlinear perturbation of the flow induced by a single steady rotlet. Lastly, the effect of an independent spin of the spheroid as it rotates was developed and assessed. It is seen that this additional spin can dramatically increase vertical fluctuation in the Lagrangian trajectories.

These studies directly tie into the observation of particle motion in actuated nano-scale fluidics, where controlled actuation of nano-rods using a magnetic force microscope has induced similar motion as the spheroids studied in the present manuscript, and additionally those studies have seen similar epicycle and orbit trajectories of micrometre and sub-micrometre scale beads (Fisher *et al.* 2006; Jing 2006). Those microscopic observations of the tracer motion are often affected by uncertainties caused by numerous factors, including the wavelength of visible light which makes direct visible observation of the nano-scale rods difficult *in vivo*. (Moreover, at present, the types of observation possible with the obstruction imposed by the magnetic force microscope makes three-dimensional imaging extremely difficult.) Even without the complexities associated with random thermal effects on these scales, these uncertainties could be greatly reduced by the availability of accurate predictive hydrodynamic theory for these geometries. For example, the presence of a strong ‘sweet spot’ in the polar amplitude of the Lagrangian trajectories just below the cone height could be used to supply missing experimental information, either about the detailed rod and cone geometry, or about the relative height of the tracers relative to the cone height. These sorts of diagnostic tools are anticipated to be useful in the developing fields of nano-fluidics.

While informative, the exact solution and its analysis presented here have numerous limitations that elicit further exploration. First, spinning rod experiments typically involve a no-slip floor at which the rod is frictionally attached. This can cause non-negligible effects. The frictional contact of the base point can be anticipated to induce an additional spin of the body around its major axis such as the independent spin we have incorporated in § 7. Unfortunately, the presence of the floor also modifies the boundary condition, and exact solutions for rotating spheroids above flat planes are surely much more difficult. Part 2 will present a slender-body theory we have developed using image charges introduced by Blake (1971). We are presently validating this asymptotic theory with table-top as well as nano-scale spinning-rod experiments. The behaviour of fluid particles in the free-space and half-space problems is qualitatively similar, but important quantitative differences caused by the no-slip floor do emerge. Lastly, the effects of thermal Brownian motion are expected to give rise to differences in the Lagrangian trajectories. With the technological advances allowing for controlled motion of bodies on nano-scales, there is the strong potential for new measurements to lead to improved understanding of fluctuating hydrodynamic systems. The availability of exact, or asymptotic, deterministic hydrodynamic solutions merely scratches the surface of new phenomena anticipated on such small scales.

The authors wish to thank Hao Jing, Richard Superfine and Leandra Vicci, for the scientific collaboration over the past several years. In particular, we especially thank Hao Jing and Richard Superfine for sharing with us their nanoscale hydrodynamics experiments involving rods sweeping upright cones, in which they observed the epicycle motion of tracers found in our theoretical study. We also wish to thank the UNC RMX Project for stimulating scientific discussion which gave rise to many of the observations we have made in this mathematical work. Additionally, we wish to acknowledge the UNC Virtual Lung project and the UNC Cystic Fibrosis Center for providing much of the motivaton for the present work. We further wish to thank David Adalsteinsson for tremendous help with his Data Tank program which was instrumental in all of the high-resolution graphics. Lastly, we wish to thank the National Science Foundation for its support of this research. Specifically, the work of R. C. was partially supported by NSF DMS-0104329 and NSF DMS-0509423, the work of T. J. L. was fully supported by NSF DMS-0308687 and the National Science Foundation Research Training Grant, RTG NSF DMS-0502266, and the work of R. M. M. was partially supported by NSF DMS-0308687. All authors gratefully acknowledge NSF for support through research training grant RTG NSF DMS-0502266. Computational work was supported by NSF DMS-SCREMS 042241.

Appendix A. Singularity theory

Determining solutions for Stokes flow is difficult in general for arbitrary boundary conditions. One analytical method available for obtaining solutions is singularity theory (Batchelor 1970; Chwang & Wu 1975; Wu 1978; Kim 1986; Pozrikidis 1997). The basis is to construct solutions to particular boundary-value problems by superposition of fundamental solutions. Fundamental solutions are found by solving Stokes equations

$$\left.\begin{aligned} \mu\nabla^2\boldsymbol{u} + \boldsymbol{f} &= \nabla p, \\ \nabla\cdot\boldsymbol{u} &= 0, \end{aligned}\right\} \tag{A 1}$$

which are singularly forced by $\boldsymbol{f}$ in an unbounded fluid. The superposition is constructed so that the boundary conditions are satisfied either exactly or approximately. The difficulty in the method lies in choosing the correct combination of fundamental solutions and their spatial distributions.

The primary fundamental solution to Stokes equations is the Stokeslet. The Stokeslet is associated to the singular point force $\boldsymbol{f}_s = 8\pi\mu\,\boldsymbol{\alpha}\,\delta(\boldsymbol{x})$ applied, here, at the origin where $\delta(\boldsymbol{x})$ is the three-dimensional Dirac delta-function. The vector $\boldsymbol{\alpha}$ characterizes the Stokeslet strength in magnitude and direction. The Stokeslet velocity field is given as

$$\boldsymbol{u}_S(\boldsymbol{x};\boldsymbol{\alpha}) = \frac{\boldsymbol{\alpha}}{|\boldsymbol{x}|} + \frac{(\boldsymbol{\alpha}\cdot\boldsymbol{x})\boldsymbol{x}}{|\boldsymbol{x}|^3}. \tag{A 2}$$

Since the Stokes equations are linear, any derivative of the Stokeslet solution is also a fundamental solution. Hence, higher-order fundamental solutions to the Stokes equations can be obtained through differentiation of $\boldsymbol{u}_S$ and p_S. The corresponding fundamental singularity is found as that same derivative of $\boldsymbol{f}_S$. The Stokes doublet is such a higher-order singularity and its velocity field is defined by

$$\begin{aligned}\boldsymbol{u}_{SD}(\boldsymbol{x};\boldsymbol{\alpha},\boldsymbol{\beta}) &= (\boldsymbol{\beta}\cdot\nabla)\boldsymbol{u}_S(\boldsymbol{x};\boldsymbol{\alpha})\\ &= \frac{(\boldsymbol{\alpha}\times\boldsymbol{\beta})\times\boldsymbol{x}}{|\boldsymbol{x}|^3} - \frac{(\boldsymbol{\alpha}\cdot\boldsymbol{\beta})\boldsymbol{x}}{|\boldsymbol{x}|^3} + \frac{3(\boldsymbol{\alpha}\cdot\boldsymbol{x})(\boldsymbol{\beta}\cdot\boldsymbol{x})\boldsymbol{x}}{|\boldsymbol{x}|^5}.\end{aligned} \tag{A 3}$$

This singularity can be further decomposed to form additional solutions. For example, the symmetric component of the Stokes doublet with respect to its strengths gives a fundamental solution known as the stresslet. The stresslet velocity field is given as

$$\begin{aligned}\boldsymbol{u}_{SS}(\boldsymbol{x};\boldsymbol{\alpha},\boldsymbol{\beta}) &= \tfrac{1}{2}(\boldsymbol{u}_{SD}(\boldsymbol{x};\boldsymbol{\alpha},\boldsymbol{\beta}) + \boldsymbol{u}_{SD}(\boldsymbol{x};\boldsymbol{\beta},\boldsymbol{\alpha}))\\ &= -\frac{(\boldsymbol{\alpha}\cdot\boldsymbol{\beta})\boldsymbol{x}}{|\boldsymbol{x}|^3} + \frac{3(\boldsymbol{\alpha}\cdot\boldsymbol{x})(\boldsymbol{\beta}\cdot\boldsymbol{x})\boldsymbol{x}}{|\boldsymbol{x}|^5}.\end{aligned} \tag{A 4}$$

Further, the antisymmetric component of the Stokes doublet is a singularity known as the rotlet. The rotlet velocity field is found to be

$$\begin{aligned}\boldsymbol{u}_R(\boldsymbol{x};\boldsymbol{\gamma}) &= \tfrac{1}{2}(\boldsymbol{u}_{SD}(\boldsymbol{x};\boldsymbol{\alpha},\boldsymbol{\beta}) - \boldsymbol{u}_{SD}(\boldsymbol{x};\boldsymbol{\beta},\boldsymbol{\alpha}))\\ &= \frac{\boldsymbol{\gamma}\times\boldsymbol{x}}{|\boldsymbol{x}|^3},\end{aligned} \tag{A 5}$$

where $\boldsymbol{\gamma} = \boldsymbol{\alpha}\times\boldsymbol{\beta}$.

Another fundamental solution which plays a role in low-Reynolds-number flows is the point-source dipole. It is constructed by considering an irrotational velocity field and its associated scalar potential

$$\boldsymbol{u} = \nabla\phi, \tag{A 6}$$

and by placing a point source of mass in the flow field,

$$\nabla\cdot\boldsymbol{u} = \delta(\boldsymbol{x}), \tag{A 7}$$

located, here, at the origin. The scalar potential is then given as the fundamental solution of the Laplacian and the associated point-source dipole velocity field is found as

$$\begin{aligned}\boldsymbol{u}_D(\boldsymbol{x};\boldsymbol{\eta}) &= \nabla\left(\nabla\cdot\frac{\boldsymbol{\eta}}{|\boldsymbol{x}|}\right)\\ &= -\frac{\boldsymbol{\eta}}{|\boldsymbol{x}|^3} + \frac{3\,(\boldsymbol{\eta}\cdot\boldsymbol{x})\,\boldsymbol{x}}{|\boldsymbol{x}|^5}.\end{aligned} \tag{A 8}$$

The point-source dipole pressure field is constant. Again, derivatives of the point-source dipole are also fundamental solutions.

Appendix B. From the body- to the laboratory-frame

Let $\boldsymbol{x}_0$ lie on the boundary of the spheroid $\partial\vartheta$ in (3.1) which is centred about the origin lying on the x-axis. Suppose we can obtain the velocity field $\boldsymbol{u}(\boldsymbol{x})$ whose solution satisfies

$$\left.\begin{aligned} \boldsymbol{u}(\boldsymbol{x}_0) &= \boldsymbol{0}, \\ \lim_{\boldsymbol{x}\to\infty} \boldsymbol{u}(\boldsymbol{x}) &= \omega\,(y, -x, 0). \end{aligned}\right\} \tag{B 1}$$

As mentioned in § 3.1, the solution to this boundary value problem is one in which the spheroid is fixed in a rotating background flow $\boldsymbol{U}(\boldsymbol{x}) = \omega\,(y, -x, 0)$. Further suppose we are interested in the fluid motion induced by a body rotating in a fluid which is otherwise at rest.

Consider a spheroid lying in the (x, y)-plane and sweeping out a circle rather than a double cone. That is, let the cone angle $\kappa = \pi/2$. Suppose the boundary of the body is rotating by an angle $\vartheta(t)$. Then, at each instance of time t, the spheroid is found at

$$\frac{(x\cos\vartheta(t) - y\sin\vartheta(t))^2}{a^2} + \frac{(x\sin\vartheta(t) + y\cos\vartheta(t))^2 + z^2}{b^2} = 1. \tag{B 2}$$

This is obtained by observing that each point on $\partial\vartheta$ is rotated by the unsteady orthogonal transformation

$$\boldsymbol{R}_\vartheta = \begin{pmatrix} \cos\vartheta(t) & -\sin\vartheta(t) & 0 \\ \sin\vartheta(t) & \cos\vartheta(t) & 0 \\ 0 & 0 & 1 \end{pmatrix}. \tag{B 3}$$

Define $\boldsymbol{x}'(t) = R_\vartheta(t)\boldsymbol{x}$. Then the velocity field in the rotated $\boldsymbol{x}'$-coordinate system becomes

$$\begin{aligned} \boldsymbol{u}'(\boldsymbol{x}') &= \frac{\mathrm{d}\boldsymbol{x}'}{\mathrm{d}t} \\ &= \left.\frac{\mathrm{d}(R_\vartheta \boldsymbol{x})}{\mathrm{d}t}\right|_{\boldsymbol{x}=R_\vartheta^T\boldsymbol{x}'} \\ &= \left.\left(\dot{R}_\vartheta \boldsymbol{x} + R_\vartheta \frac{\mathrm{d}\boldsymbol{x}}{\mathrm{d}t}\right)\right|_{\boldsymbol{x}=R_\vartheta^T\boldsymbol{x}'} \\ &= \dot{R}_\vartheta R_\vartheta^T \boldsymbol{x}' + R_\vartheta \boldsymbol{u}\left(R_\vartheta^T \boldsymbol{x}'\right) \\ &= -\boldsymbol{U}(\boldsymbol{x}') + R_\vartheta \boldsymbol{u}\left(R_\vartheta^T \boldsymbol{x}'\right). \end{aligned} \tag{B 4}$$

Hence, for $\boldsymbol{x}_0'$ on the boundary of this moving spheriod $\partial\vartheta'$ defined in (B 2),

$$\left.\begin{aligned} \boldsymbol{u}'(\boldsymbol{x}_0') &= \omega\,(-y',\, x',\, 0) \\ \lim_{\boldsymbol{x}'\to\infty} \boldsymbol{u}'(\boldsymbol{x}') &= 0, \end{aligned}\right\} \tag{B 5}$$

by design of $\boldsymbol{u}(\boldsymbol{x})$ in (B 1). Thus, the velocity field $\boldsymbol{u}'(\boldsymbol{x}')$ in the laboratory frame is found simply as a transformation of the body-frame velocity field $\boldsymbol{u}(\boldsymbol{x})$, and $\boldsymbol{u}'(\boldsymbol{x}')$ becomes the velocity field due to a spheroid sweeping out a circle in the (x', y')-plane in a fluid which is otherwise at rest.

To obtain the sweeping for a double cone motion, we must consider tilting the body, say in the (x, z)-plane, before moving to the rotating laboratory frame. Consider the boundary conditions examined by Chwang & Wu (1975) in (B 1) but, instead, for a tilted body fixed in a background rotating flow. The boundary of a spheroid tilted in the (x, z)-plane by an angle κ from the z-axis is given as

$$\frac{(x\sin\kappa - z\cos\kappa)^2}{a^2} + \frac{y^2 + (x\sin\kappa + z\cos\kappa)^2}{b^2} = 1. \tag{B 6}$$

This is obtained by observing that each point on $\partial\vartheta$ is tilted by the steady orthogonal transformation

$$\boldsymbol{R}_\kappa = \begin{pmatrix} \sin\kappa & 0 & -\cos\kappa \\ 0 & 1 & 0 \\ \cos\kappa & 0 & \sin\kappa \end{pmatrix}. \tag{B 7}$$

Note that this transformation provides no moving boundary.

Define $\widetilde{\boldsymbol{x}} = R_\kappa \boldsymbol{x}$. Then the velocity field in the tilted $\widetilde{\boldsymbol{x}}$-coordinate system becomes

$$\begin{aligned} \widetilde{\boldsymbol{u}}(\widetilde{\boldsymbol{x}}) &= \frac{\mathrm{d}\widetilde{\boldsymbol{x}}}{\mathrm{d}t} \\ &= \left.\frac{\mathrm{d}(R_\kappa \boldsymbol{x})}{\mathrm{d}t}\right|_{x = R_\kappa^T \widetilde{x}} \\ &= R_\kappa \boldsymbol{u}\left(R_\kappa^T \widetilde{\boldsymbol{x}}\right). \end{aligned} \tag{B 8}$$

By constructing a velocity field $\boldsymbol{u}(\boldsymbol{x})$ which satisfies

$$\left.\begin{aligned} &\boldsymbol{u}(\boldsymbol{x}_0) = \boldsymbol{0}, \\ &\lim_{\boldsymbol{x}\to\infty} \boldsymbol{u}(\boldsymbol{x}) = R_\kappa^T \boldsymbol{U}(R_\kappa \boldsymbol{x}), \end{aligned}\right\} \tag{B 9}$$

where $\boldsymbol{x}$ is defined in the body frame with the spheroid lying on the axis, it is readily found, through (B 8), that for $\widetilde{\boldsymbol{x}}_0$ on the boundary of this tilted spheriod $\widetilde{\partial\vartheta}$ defined in (B 6),

$$\left.\begin{aligned} &\widetilde{\boldsymbol{u}}(\widetilde{\boldsymbol{x}}_0) = \boldsymbol{0}, \\ &\lim_{\widetilde{\boldsymbol{x}}\to\infty} \widetilde{\boldsymbol{u}}(\widetilde{\boldsymbol{x}}) = \boldsymbol{U}(\widetilde{\boldsymbol{x}}). \end{aligned}\right\} \tag{B 10}$$

Hence, $\widetilde{\boldsymbol{u}}(\widetilde{\boldsymbol{x}})$ describes the velocity field due to a body tilted in the $(\widetilde{x}, \widetilde{z})$-plane fixed in a rotating background flow, and, more specifically, fixed in a rotation of the $(\widetilde{x}, \widetilde{y})$-plane. The far-field boundary condition provided by (B 9) is the appropriate one for such a fluid motion.

Recall that the goal is to obtain the fluid motion due to a tilted spheroid which rotates according to the boundary conditions given in (B 5). We would like to accomplish this goal by using the solution strategy initiated in the body frame by Chwang & Wu (1975). To do so, we adopt the following procedure.

1. *In the body frame*
   Solve the boundary-value problem in (B 9). This provides the fluid motion due to a spheroid lying on the x-axis embedded in the far-field rotation $R_\kappa^T \boldsymbol{U}(R_\kappa \boldsymbol{x})$.

2. *Transform the body frame*
   Apply the steady transformation R_κ. This provides the fluid motion due to a tilted spheroid embedded in the rotation of a plane. This rotation is more specifically $\boldsymbol{U}(\boldsymbol{x}) = \omega(y, -x, 0)$.

3. *Move to the laboratory frame*
   Apply the unsteady transformation $R_\vartheta = R_\vartheta(t)$. This provides the fluid motion due to a tilted spheroid rotating in a fluid otherwise at rest. The

resulting boundary condition for a spheroid which sweeps out a double cone is provided in (B 5).

This strategy is more precisely defined by considering the transformation $\boldsymbol{x}^*(t) = R_\vartheta R_\kappa \boldsymbol{x}$. At each instance of time t, this change of variables places the tilted rotating spheroid at

$$\frac{((x\sin\kappa - z\cos\kappa)\cos\vartheta(t) - y\sin\vartheta(t))^2}{a^2} + \frac{((x\sin\kappa - z\cos\kappa)\sin\vartheta(t) + y\cos\vartheta(t))^2 + (x\cos\kappa + z\sin\kappa)^2}{b^2} = 1. \tag{B 11}$$

Assuming we can solve the boundary-value problem in Step 1, the velocity $\boldsymbol{u}^*(\boldsymbol{x}^*)$ in the laboratory frame is found with the formulation of (B 4) in mind. That is, the velocity field in the $\boldsymbol{x}^*$-coordinate system becomes

$$\begin{aligned} \boldsymbol{u}^*(\boldsymbol{x}^*) &= \frac{\mathrm{d}\boldsymbol{x}^*}{\mathrm{d}t} \\ &= \left.\frac{\mathrm{d}(R_\vartheta R_\kappa \boldsymbol{x})}{\mathrm{d}t}\right|_{\boldsymbol{x}=R_\kappa^T R_\vartheta^T \boldsymbol{x}^*} \\ &= -\boldsymbol{U}(\boldsymbol{x}^*) + R_\vartheta R_\kappa \boldsymbol{u}\left(R_\kappa^T R_\vartheta^T \boldsymbol{x}^*\right). \end{aligned} \tag{B 12}$$

Let $\boldsymbol{x}_0^*$ lie on the boundary of the tilted rotating body $\partial\vartheta^*$ in (B 11). The construction of a solution to Stokes equations which satisfies the boundary conditions

$$\left.\begin{aligned} \boldsymbol{u}^*(\boldsymbol{x}_0^*) = \boldsymbol{U}^*(\boldsymbol{x}_0^*), \\ \lim_{\boldsymbol{x}^*\to\infty} \boldsymbol{u}^*(\boldsymbol{x}^*) = \boldsymbol{0}, \end{aligned}\right\} \tag{B 13}$$

is verified through the definition in (B 12) and the boundary conditions imposed on $\boldsymbol{u}(\boldsymbol{x})$.

Appendix C. Singularity distribution

Define $\boldsymbol{e}_x = (1, 0, 0)$, $\boldsymbol{e}_y = (0, 1, 0)$, and $\boldsymbol{e}_z = (0, 0, 1)$ to be basis elements of $\mathbb{R}^3$. Let $\boldsymbol{x}_0$ lie on the boundary of the spheroid in (3.1) which is centred at the origin lying on the x-axis. Then the velocity fields which satisfy $\boldsymbol{u}^i(\boldsymbol{x}_0) = 0$ for $i = 1, 2, 3$ and

$$\lim_{\boldsymbol{x}\to\infty} \boldsymbol{u}^1(\boldsymbol{x}) = \omega\ y\sin\kappa\ \boldsymbol{e}_x, \tag{C 1a}$$

$$\lim_{\boldsymbol{x}\to\infty} \boldsymbol{u}^2(\boldsymbol{x}) = -\omega\ x\sin\kappa\ \boldsymbol{e}_y, \tag{C 1b}$$

$$\lim_{\boldsymbol{x}\to\infty} \boldsymbol{u}^3(\boldsymbol{x}) = \omega\ z\cos\kappa\ \boldsymbol{e}_y, \tag{C 1c}$$

are provided by Chwang & Wu (1975) as

$$\begin{aligned} \boldsymbol{u}^1(\boldsymbol{x}) = \omega\ \sin\kappa \Bigg(y\ \boldsymbol{e}_x + \int_{-c}^{c} (c^2 - s^2)[\alpha_1\ \boldsymbol{u}_{SS}(\boldsymbol{x} - \boldsymbol{s}; \boldsymbol{e}_x, \boldsymbol{e}_y) + \gamma_1\ \boldsymbol{u}_R(\boldsymbol{x} - \boldsymbol{s}; \boldsymbol{e}_z)]\,\mathrm{d}s \\ +\ \beta_1 \int_{-c}^{c} (c^2 - s^2)^2 \frac{\partial}{\partial y} \boldsymbol{u}_D(\boldsymbol{x} - \boldsymbol{s}; \boldsymbol{e}_x)\,\mathrm{d}s \Bigg) \end{aligned} \tag{C 2a}$$

$$\begin{aligned} \boldsymbol{u}^2(\boldsymbol{x}) = \omega\ \sin\kappa \Bigg(-x\ \boldsymbol{e}_y + \int_{-c}^{c} (c^2 - s^2)[\alpha_2\ \boldsymbol{u}_{SS}(\boldsymbol{x} - \boldsymbol{s}; \boldsymbol{e}_x, \boldsymbol{e}_y) + \gamma_2\ \boldsymbol{u}_R(\boldsymbol{x} - \boldsymbol{s}; \boldsymbol{e}_z)]\,\mathrm{d}s \\ +\ \beta_2 \int_{-c}^{c} (c^2 - s^2)^2 \frac{\partial}{\partial y} \boldsymbol{u}_D(\boldsymbol{x} - \boldsymbol{s}; \boldsymbol{e}_x)\,\mathrm{d}s \Bigg) \end{aligned} \tag{C 2b}$$

$$
\begin{aligned}
\boldsymbol{u}^3(\boldsymbol{x}) = \omega\ \cos\kappa\Bigg(\ z\ \boldsymbol{e}_y\ &+ \int_{-c}^{c}(c^2-s^2)[\alpha_3\ \boldsymbol{u}_{SS}(\boldsymbol{x}-\boldsymbol{s}\,;\boldsymbol{e}_y,\boldsymbol{e}_z)+\gamma_3\ \boldsymbol{u}_R(\boldsymbol{x}-\boldsymbol{s}\,;\boldsymbol{e}_x)]\,\mathrm{d}s \\
&+\beta_3\int_{-c}^{c}(c^2-s^2)^2\frac{\partial}{\partial z}\boldsymbol{u}_D(\boldsymbol{x}-\boldsymbol{s}\,;\boldsymbol{e}_y)\,\mathrm{d}s\Bigg)
\end{aligned}
\tag{C 2c}
$$

with

$$\gamma_1 = \frac{(1-e^2)}{-2e+(1+e^2)\log\left(\dfrac{1+e}{1-e}\right)}, \tag{C 3a}$$

$$
\begin{aligned}
\alpha_1 &= \frac{4e^2}{1-e^2}\ \beta_1, \\
&= \frac{2\,e^2\,\gamma_1\left(-2e+\log\left(\dfrac{1+e}{1-e}\right)\right)}{2e(2e^2-3)+3(1-e^2)\log\left(\dfrac{1+e}{1-e}\right)},
\end{aligned}
\tag{C 3b}
$$

$$\gamma_2 = \frac{1}{-2e+(1+e^2)\log\left(\dfrac{1+e}{1-e}\right)}, \tag{C 3c}$$

$$\alpha_2 = \frac{4e^2}{1-e^2}\ \beta_2, \tag{C 3d}$$

$$= \frac{e^2\,\gamma_2\left(-2e+(1-e^2)\log\left(\dfrac{1+e}{1-e}\right)\right)}{2e(2e^2-3)+3(1-e^2)\log\left(\dfrac{1+e}{1-e}\right)}, \tag{C 3e}$$

$$\gamma_3 = \frac{1-e^2}{2\left(2e-(1-e^2)\log\left(\dfrac{1+e}{1-e}\right)\right)}, \tag{C 3f}$$

$$
\begin{aligned}
\alpha_3 &= \frac{4e^2}{1-e^2}\ \beta_3, \\
&= \frac{2\,e^2\,(1-e^2)}{2e(5e^2-3)+3(1-e^2)^2\log\left(\dfrac{1+e}{1-e}\right)}.
\end{aligned}
\tag{C 3g}
$$

The required singularities to solve these boundary-value problems are the stresslet $\boldsymbol{u}_{SS}$, the rotlet $\boldsymbol{u}_R$, and a derivative of the point-source dipole $\boldsymbol{u}_D$. A description of these fundamental solutions is provided in Appendix A.

Chwang & Wu (1975) did not provide the explicit singularity distribution for $\boldsymbol{u}^4(\boldsymbol{x})$ which satisfies

$$
\left.
\begin{aligned}
&\boldsymbol{u}^4(\boldsymbol{x}_0) = 0, \\
&\lim_{\boldsymbol{x}\to\infty}\boldsymbol{u}^4(\boldsymbol{x}) = -\omega\ y\cos\kappa\ \boldsymbol{e}_z.
\end{aligned}
\right\}
\tag{C 4}
$$

This solution is provided as a transformation of $\boldsymbol{u}^3(\boldsymbol{x})$ of the form $y \leftrightarrow z$.

Examine the singularities which comprise the solution of $\boldsymbol{u}^3(\boldsymbol{x})$ and note, from Appendix A, that the stresslet and point-source dipole singularities satisfy, respectively,

$$\left.\begin{aligned} \boldsymbol{u}_{SS}(\boldsymbol{x};\boldsymbol{\alpha},\boldsymbol{\beta}) &= \boldsymbol{u}_{SS}(\boldsymbol{x};\boldsymbol{\beta},\boldsymbol{\alpha}), \\ \frac{\partial}{\partial y}\boldsymbol{u}_D(\boldsymbol{x};\boldsymbol{e}_z) &= \frac{\partial}{\partial z}\boldsymbol{u}_D(\boldsymbol{x};\boldsymbol{e}_y). \end{aligned}\right\} \tag{C 5}$$

Recall from the same Appendix, that the rotlet singularity is defined as

$$\boldsymbol{u}_R(\boldsymbol{x};\boldsymbol{\gamma}) = \frac{\boldsymbol{\gamma}\times\boldsymbol{x}}{|\boldsymbol{x}|^3}. \tag{C 6}$$

where $\boldsymbol{\gamma} = \boldsymbol{\alpha}\times\boldsymbol{\beta}$. Thus transforming the rotlet singularity $\boldsymbol{u}_R(\boldsymbol{x}-\boldsymbol{s};\boldsymbol{e}_x)$ in $\boldsymbol{u}^3(\boldsymbol{x})$ requires that we recall that the rotlet is a fundamental solution dependent on two directions. Hence

$$\boldsymbol{u}_R(\boldsymbol{x}-\boldsymbol{s};\boldsymbol{e}_x) \equiv \boldsymbol{u}_R(\boldsymbol{x}-\boldsymbol{s};\boldsymbol{e}_y,\boldsymbol{e}_z) \tag{C 7}$$

is transformed to

$$\boldsymbol{u}_R(\boldsymbol{x}-\boldsymbol{s};\boldsymbol{e}_z,\boldsymbol{e}_y) \equiv -\boldsymbol{u}_R(\boldsymbol{x}-\boldsymbol{s};\boldsymbol{e}_x), \tag{C 8}$$

and the velocity field for a prolate spheroid held fixed in a flow which is in the z-direction and sheared in the y-direction with the free-stream velocity $-\omega\, y\cos\kappa\ \boldsymbol{e}_z$ is

$$\begin{aligned} \boldsymbol{u}^4(\boldsymbol{x}) = \omega\ \cos\kappa\Bigg(-y\ \boldsymbol{e}_z\ + \int_{-c}^{c}(c^2-s^2)[\alpha_4\ \boldsymbol{u}_{SS}(\boldsymbol{x}-\boldsymbol{s};\boldsymbol{e}_y,\boldsymbol{e}_z) + \gamma_4\ \boldsymbol{u}_R(\boldsymbol{x};\boldsymbol{e}_x)]\,\mathrm{d}s \\ +\beta_4\int_{-c}^{c}(c^2-s^2)^2\frac{\partial}{\partial z}\boldsymbol{u}_D(\boldsymbol{x}-\boldsymbol{s};\boldsymbol{e}_y)\,\mathrm{d}s\Bigg) \end{aligned} \tag{C 9}$$

where

$$\begin{aligned} \gamma_4 &= \gamma_3 \\ &= \frac{1-e^2}{2\left(2e-(1-e^2)\log\left(\dfrac{1+e}{1-e}\right)\right)}, \end{aligned} \tag{C 10}$$

$$\begin{aligned} \alpha_4 &= -\ \alpha_3 \\ &= -\ \frac{4e^2}{1-e^2}\ \beta_3 \\ &= \frac{4e^2}{1-e^2}\ \beta_4 \\ &= \frac{2\,e^2\,(1-e^2)}{2e(3-5e^2)-3(1-e^2)^2\log\left(\dfrac{1+e}{1-e}\right)}. \end{aligned} \tag{C 11}$$

This is verified by Leiterman (2006) where the Stokes velocity solution $\boldsymbol{u}^4(\boldsymbol{x})$ defined by (C 4) is provided as the solution to an integral equation evaluated along the boundary of the spheroid

$$\frac{x^2}{a^2}+\frac{y^2+z^2}{b^2} = 1 \qquad (a > b), \tag{C 12}$$

held fixed in the far-field shear flow $-\omega\ y\cos\kappa\ \boldsymbol{e}_z$.

Appendix D. Integrals in closed form

The singularity distribution for the velocity field in (3.14) involves integrals of the stresslet $\boldsymbol{u}_{SS}$, rotlet $\boldsymbol{u}_R$ and a derivative of the point-source dipole $\boldsymbol{u}_D$ which have closed algebraic and logarithmic forms. The basic fundamental solutions mentioned are described in Appendix A. The integrals involving these singularities required for the construction of (3.14) are tabulated below. Let $\boldsymbol{s}=(s,0,0)$, $\boldsymbol{e}_x=(1,0,0)$, $\boldsymbol{e}_y=(0,1,0)$, and $\boldsymbol{e}_z=(0,0,1)$. Define

$$\left.\begin{aligned} r^2 &= x^2+y^2+z^2,\\ r_s^2 &= y^2+z^2. \end{aligned}\right\} \tag{D 1}$$

Stresslet distribution

$$\int (c^2-s^2)\,\boldsymbol{u}_{SS}(\boldsymbol{x}-\boldsymbol{s};\boldsymbol{e}_x,\boldsymbol{e}_y)\,\mathrm{d}s = \int \frac{3\,(x-s)\,y\,(c^2-s^2)}{((x-s)^2+y^2+z^2)^{5/2}}\begin{pmatrix} x-s\\ y\\ z\end{pmatrix}\mathrm{d}s. \tag{D 2}$$

(i)

$$\begin{aligned} &\int \frac{3\,(x-s)^2\,y\,(c^2-s^2)}{\left((x-s)^2+r_s^2\right)^{5/2}}\,\mathrm{d}s\\ &\quad=\frac{y\left(-c^2(x-s)^3+xr^4+3xs^2\left(x^2-3r_s^2\right)+s^3\left(-x^2+4r_s^2\right)+3s\left(-x^4+r_s^4\right)\right)}{r_s^2\,\left((x-s)^2+r_s^2\right)^{3/2}}\\ &\qquad-3y\log\left|(x-s)-\sqrt{(x-s)^2+r_s^2}\right|. \end{aligned} \tag{D 3}$$

(ii)

$$\begin{aligned} &\int \frac{3\,(x-s)\,y\,(c^2-s^2)}{((x-s)^2+r_s^2)^{5/2}}\begin{pmatrix} y\\ z\end{pmatrix}\mathrm{d}s\\ &\quad=\frac{-2x(x^3-s^3)-4x^2r_s^2+6sxr^2-3s^2(x^2+r^2)+r_s^2\left(c^2-2r_s^2\right)}{r_s^2\left((x-s)^2+r_s^2\right)^{3/2}}\begin{pmatrix} y^2\\ yz\end{pmatrix}. \end{aligned} \tag{D 4}$$

Rotlet distributions

$$\int (c^2-s^2)\,\boldsymbol{u}_R(\boldsymbol{x}-\boldsymbol{s};\boldsymbol{e}_z)\,\mathrm{d}s = \int \frac{(c^2-s^2)}{((x-s)^2+y^2+z^2)^{3/2}}\begin{pmatrix} -y\\ x-s\\ 0\end{pmatrix}\mathrm{d}s, \tag{D 5a}$$

$$\int (c^2-s^2)\,\boldsymbol{u}_R(\boldsymbol{x}-\boldsymbol{s};\boldsymbol{e}_x)\,\mathrm{d}s = \int \frac{(c^2-s^2)}{((x-s)^2+y^2+z^2)^{3/2}}\begin{pmatrix} 0\\ -z\\ y\end{pmatrix}\mathrm{d}s. \tag{D 5b}$$

(i)

$$\begin{aligned} \int \frac{(c^2-s^2)\,(x-s)}{\left((x-s)^2+r_s^2\right)^{3/2}}\,\mathrm{d}s &= \frac{c^2+s^2-4sx+2r^2}{\sqrt{(x-s)^2+r_s^2}}\\ &\quad+2x\log\left|(x-s)-\sqrt{(x-s)^2+r_s^2}\right|. \end{aligned} \tag{D 6}$$

(ii)

$$\int \frac{(c^2-s^2)}{\left((x-s)^2+r_s^2\right)^{3/2}}\begin{pmatrix} y \\ z \end{pmatrix}\mathrm{d}s$$
$$= \left[\frac{-c^2(x-s)+s\left(-x^2+r_s^2\right)-xr^2}{r_s^2\sqrt{(x-s)^2+r_s^2}}-\log\left|(x-s)-\sqrt{(x-s)^2+r_s^2}\right|\right]\begin{pmatrix} y \\ z \end{pmatrix}. \tag{D 7}$$

Point-source quadripole distribution

$$\int (c^2-s^2)^2\frac{\partial}{\partial y}\boldsymbol{u}_D(\boldsymbol{x}-\boldsymbol{s};\boldsymbol{e}_x)\,\mathrm{d}s$$
$$= \int \frac{3\,(c^2-s^2)^2}{((x-s)^2+y^2+z^2)^{5/2}}\begin{pmatrix} y \\ x-s \\ 0 \end{pmatrix}\mathrm{d}s$$
$$- \int \frac{15\,(c^2-s^2)^2\,(x-s)\,y}{((x-s)^2+y^2+z^2)^{7/2}}\begin{pmatrix} x-s \\ y \\ z \end{pmatrix}\mathrm{d}s. \tag{D 8}$$

(i)

$$\int \frac{3\,(c^2-s^2)^2(x-s)}{\left((x-s)^2+r_s^2\right)^{5/2}}\,\mathrm{d}s$$
$$= \frac{(c^4-3s^4)r_s^2-4s^3x\left(x^2-7r_s^2\right)+4r^4\left(x^2-2r_s^2\right)-12sx\left(x^4-2x^2r_s^2-3r_s^4\right)}{r_s^2\left((x-s)^2+r_s^2\right)^{3/2}}$$
$$+\ \frac{12s^2\left(x^4-4x^2r_s^2-r_s^4\right)+2c^2(2s^3x+6sxr^2-2r^4-3s^2(x^2+r^2))}{r_s^2\left((x-s)^2+r_s^2\right)^{3/2}}$$
$$-12x\log\left|(x-s)-\sqrt{(x-s)^2+r_s^2}\right|. \tag{D 9}$$

(ii)

$$\int\frac{3\,(c^2-s^2)^2y}{\left((x-s)^2+r_s^2\right)^{5/2}}\,\mathrm{d}s$$
$$= \frac{-c^4(x-s)\left(2(x-s)^2+3r_s^2\right)+3s\left(2x^6+7x^4r_s^2+4x^2r_s^4-r_s^6\right)+2s^3\left(x^4+3x^2r_s^2-2r_s^4\right)}{r_s^4\left((x-s)^2+r_s^2\right)^{3/2}}$$
$$-\frac{6s^2x^3\left(x^2+3r_s^2\right)+xr^4\left(2x^2+5r_s^2\right)+2c^2(6sx^2r^2-2xr^4+(s^3-3s^2x)(x^2+r^2))}{r_s^4\left((x-s)^2+r_s^2\right)^{3/2}}$$
$$+3y\log\left|(x-s)-\sqrt{(x-s)^2+r_s^2}\right|. \tag{D 10}$$

(iii)

$$\int\frac{-15\,(c^2-s^2)^2\,(x-s)^2\,y}{\left((x-s)^2+r_s^2\right)^{7/2}}\,\mathrm{d}s$$
$$= \frac{y(2c^2(x-s)\left(c^2-2x^2-3r_s^2\right)+(x-s)\left(2x^4+18x^2r_s^2\right)+23sr_s^4+37xr_s^4)}{r_s^4\,\sqrt{(x-s)^2+r_s^2}}$$

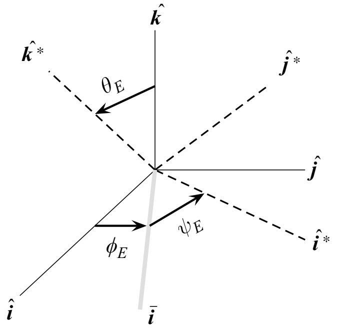

FIGURE 26. The Euler angles ϕ_E, θ_E, ψ_E specify general rigid-body rotations.

$$
\begin{aligned}
&+\frac{3y\left(c^4(s-x)+s\left(x^4-6x^2r_s^2+r_s^4\right)-x\left(x^4-2x^2r_s^2-3r_s^4\right)-2c^2\left(s\left(x^2-r_s^2\right)-xr^2\right)\right)}{\left((x-s)^2+r_s^2\right)^{5/2}}\\
&-\frac{y\left(c^4(s-x)+s\left(x^4-36x^2r_s^2+11r_s^4\right)+x\left(-x^4+16x^2r_s^2+29r_s^4\right)\right)}{r_s^2\left((x-s)^2+r_s^2\right)^{3/2}}\\
&+\frac{y\left(2c^2\left(x\left(x^2+4r_s^2\right)+s\left(-x^2+6r_s^2\right)\right)\right)}{r_s^2\left((x-s)^2+r_s^2\right)^{3/2}}\\
&-15y\log\left|(x-s)-\sqrt{(x-s)^2+r_s^2}\right|. \qquad \text{(D 11)}
\end{aligned}
$$

(iv)

$$
\begin{aligned}
&\int \frac{15\,(c^2-s^2)^2\,(x-s)\,y}{((x-s)^2+y^2+z^2)^{7/2}}\begin{pmatrix} y\\ z\end{pmatrix}\mathrm{d}s\\
&\quad=\left[\frac{8x(x-s)(c^2-x^2)-12x(x-s)r_s^2-15r_s^2-30y^2z^2}{r_s^4\sqrt{(x-s)^2+r_s^2}}\right.\\
&\qquad-\frac{3\left(c^4-3x^4-2x^2r_s^2+r_s^4+4sx\left(x^2-r_s^2\right)+2c^2(-2sx+r^2)\right)}{\left((x-s)^2+r_s^2\right)^{5/2}}\\
&\qquad\left.+\frac{2\left(-2x^4-3x^2r_s^2+5r_s^4+2sx\left(x^2-6r_s^2\right)+c^2\left(-2sx+2x^2+5r_s^2\right)\right)}{r_s^2\left((x-s)^2+r_s^2\right)^{3/2}}\right]\begin{pmatrix} y^2\\ yz\end{pmatrix}. \qquad \text{(D 12)}
\end{aligned}
$$

Appendix E. Euler angles and an additional rotation

The boundary condition on the spheroid in (7.10) can more specifically be provided as

$$\boldsymbol{U}^*(\boldsymbol{x}^*)+\boldsymbol{V}^*(\boldsymbol{x}^*)=\boldsymbol{\Omega}\times\boldsymbol{x}^* \qquad \text{(E 1)}$$

where

$$\boldsymbol{\Omega}=\begin{pmatrix}\dot{\sigma}\,\sin\kappa\,\cos\vartheta(t)\\ \dot{\sigma}\,\sin\kappa\,\sin\vartheta(t)\\ \omega+\dot{\sigma}\,\cos\kappa\end{pmatrix} \qquad \text{(E 2)}$$

is the angular velocity vector.

General rigid-body rotations can be specified through three Euler angles ϕ_E, θ_E, ψ_E (Goldstein 1950). The motion is provided in terms of three rotations.

1. Rotation through an angle ϕ_E about the axis $\hat{\boldsymbol{i}}$, $\hat{\boldsymbol{j}}$, $\hat{\boldsymbol{k}}$.
2. Rotation through an angle θ_E about the new $\hat{\boldsymbol{i}}$ axis $\bar{\boldsymbol{i}}$.
3. Rotation through an angle ψ_E about the new $\hat{\boldsymbol{k}}$ axis $\hat{\boldsymbol{k}}^*$.

The Euler angles specify the position of the body by providing three orthogonal directions $\hat{\boldsymbol{i}}^*$, $\hat{\boldsymbol{j}}^*$, $\hat{\boldsymbol{k}}^*$ defined relative to the body. This defines a body coordinate system and the description is shown in figure 26. The orientation of the $\hat{\boldsymbol{i}}$, $\hat{\boldsymbol{j}}$, $\hat{\boldsymbol{k}}$ system relative to the $\hat{\boldsymbol{i}}^*$, $\hat{\boldsymbol{j}}^*$, $\hat{\boldsymbol{k}}^*$ system is completely determined by ϕ_E, θ_E, ψ_E. The transformation from the fixed coordinate system to the body coordinate system is provided by

$$S = S_{\psi_E}\, S_{\theta_E}\, S_{\phi_E}, \tag{E 3}$$

where

$$S_{\phi_E} = \begin{pmatrix} \cos\phi_E & \sin\phi_E & 0 \\ -\sin\phi_E & \cos\phi_E & 0 \\ 0 & 0 & 1 \end{pmatrix}, \quad S_{\theta_E} = \begin{pmatrix} 1 & 0 & 0 \\ 0 & \cos\theta_E & \sin\theta_E \\ 0 & -\sin\theta_E & \cos\theta_E \end{pmatrix}, \tag{E 4a, b}$$

$$S_{\psi_E} = \begin{pmatrix} \cos\psi_E & \sin\psi_E & 0 \\ -\sin\psi_E & \cos\psi_E & 0 \\ 0 & 0 & 1 \end{pmatrix}. \tag{E 4c}$$

The angular velocity vector

$$\bar{\boldsymbol{\Omega}} \equiv \begin{pmatrix} \Omega_1 \\ \Omega_2 \\ \Omega_3 \end{pmatrix} \tag{E 5}$$

of the body relative to the axis $\hat{\boldsymbol{i}}$, $\hat{\boldsymbol{j}}$, $\hat{\boldsymbol{k}}$ is

$$S^T \dot{S} = \begin{pmatrix} 0 & \Omega_3 & -\Omega_2 \\ -\Omega_3 & 0 & \Omega_1 \\ \Omega_2 & -\Omega_1 & 0 \end{pmatrix}, \tag{E 6}$$

and it can be expressed in terms of the rate of change of the Euler angles as

$$\bar{\boldsymbol{\Omega}} = \begin{pmatrix} 0 \\ 0 \\ 1 \end{pmatrix} \dot{\phi_E} + \begin{pmatrix} \cos\phi_E \\ \sin\phi_E \\ 0 \end{pmatrix} \dot{\theta_E} + \begin{pmatrix} \sin\theta_E \sin\phi_E \\ -\sin\theta_E\cos\phi_E \\ \cos\theta_E \end{pmatrix} \dot{\psi_E}. \tag{E 7}$$

The Euler angles for the boundary condition in (E 1) which represents a body revolving about its major axis as it sweeps out a cone are as follows

(i) $\phi_E = \vartheta(t) + \pi/2$.

(This is a time-dependent rotation of the spheroid in the $(\hat{\boldsymbol{i}}, \hat{\boldsymbol{j}})$-plane with $\pi/2$ signifying that the initial orientation of the tilted body in the * frame is in the $(\hat{\boldsymbol{i}}^*, \hat{\boldsymbol{k}}^*)$-plane.)

(ii) $\theta_E = \kappa$.

(This is a steady rotation which tilts the spheroid by an angle κ in the $(\bar{\boldsymbol{i}}, \hat{\boldsymbol{k}})$-plane.)

(iii) $\psi_E = \sigma(t)$.

(This is a time-dependent rotation about the major axis of the tilted spheroid sweeping out a cone, which is aligned with the $\hat{\boldsymbol{k}}^*$-axis.)

As expected, we have

$$\bar{\boldsymbol{\Omega}} = \begin{pmatrix} 0 \\ 0 \\ 1 \end{pmatrix} \omega + \begin{pmatrix} \sin\kappa \cos\vartheta(t) \\ \sin\kappa \sin\vartheta(t) \\ \cos\kappa \end{pmatrix} \dot{\sigma} = \boldsymbol{\Omega}. \tag{E 8}$$

REFERENCES

Afzelius, B. A. 1976 A human syndrome caused by immotile cilia. *Science* **193**, 317–319.

Bajer, K. & Moffat, H. K. 1990 On a class of steady confined Stokes flows with chaotic streamlines. *J. Fluid Mech.* **212**, 337–363.

Batchelor, G. K. 1970 Slender-body theory for particle of arbitrary cross-section in Stokes flow. *J. Fluid Mech.* **44**, 419–440.

Blake, J. R. 1971 A note on the image system for a Stokeslet in a no slip boundary. *Proc. Camb. Phil. Soc.* **70**, 303–310.

Chu, S. 1991 Laser manipulation of atoms and particles. *Science* **253**, 861–866.

Chwang, A. T. & Wu, T. Y. 1975 Hydrodynamics of low-Renolds-number flow. Part 2. Singularity method for Stokes flow. *J. Fluid Mech.* **67**, 787–815.

Edwardes, D. 1892 Steady motion of a viscous liquid in which an ellipsoid is constrained to rotate about a principal axis. *Q. J. Maths* **26**, 70–78.

Fisher, J. K., Cribb, J., Desai, K. V., Vicci, L., Wilde, B., Keller, K., Taylor, R. M., Haase, J., Bloom, K., O'Brien, E. T. & Superfine, R. 2006 Thin-foil magnetic force system for high-numerical-aperature microscopy. *Rev. Sci. Instrum.* **27**, 2.

Fulford, G. R. & Blake, J. R. 1986 Muco-ciliary transport in the lung. *J. Theor. Biol.* **121**, 381–402.

Goldstein, H. 1950 *Classical Mechanics.* Addison–Wesley.

Hancock, G. J. 1953 The self-propulsion of microscopic organisms through liquids. *Proc. R. Soc.* A **217**, 96–121.

Hirokawa, N. 2000 Stirring up development with the heterotrimeric kinesin KIF3. *Traffic* **1**, 29–34.

Jing, H. 2006 Manipulating nano-scale devices: a new tunable assembly method for nano-scale fluid dynamics. PhD thesis. University of North Carolina.

Kartagener, M. 1933 Zur Pathogenese der Bronchiektasien. I. Mitteilung Bronchiektasien bei Situs viscerum inversus. *Beitr. Klin. Tuberk.* **83**, 498–501.

Kim, S. 1986 Singularity solutions for ellipsoids in low-Reynolds-number flows: with applications to the calculation of hydrodynamic interactions in suspensions of ellipsoids. *Intl J. Multiphase Flow* **12**, 469–491.

Kroujiline, D. & Stone, H. A. 1999 Chaotic streamlines in steady bounded three-dimensional Stokes flows. *Physica* D **130**, 105–132.

Leiterman, T. J. 2006 Exact and asymptotic low Reynolds, time-varying solutions for spinning rods and a comparison to experiments on the micro and macroscale. PhD thesis. University of North Carolina.

Matsui, H., Randell, S. H., Peretti, S. W., Davis, C. W. & Boucher, R. C. 1998 Coordinate clearance of periciliary liquid and mucin from airway surfaces. *J. Clin. Invest.* **102**, 1125–1131.

Nonaka, S., Shiratori, H., Saijoh, Y. & Hamada, H. 2002 Singularity solutions for ellipsoids in low-Reynolds-number flows: with applications to the calculation of hydrodynamic interactions in suspensions of ellipsoids. *Intl J. Multiphase Flow* **12**, 469–491.

Perkins, T. T., Smith, D. E. & Chu, S. 1999 Single-polymer dynamics in steady shear flow. *Science* **283**, 1724–1727.

Pozrikidis, C. 1997 *Introduction to Theoretical and Computational Fluid Dynamics.* Oxford University Press.

Sanders, J. A. & Verhulst, F. 1985 *Averaging Methods in Nonlinear Dynamical Systems.* Springer.

Sleigh, M. A., Blake, J. R. & Liron, N. 1988 The propulsion of mucus by cilia. *Am. Rev. Respir. Dis.* **137**, 726–741.

Smith, D. E., Babcock, H. P. & Chu, S. 1997 Single-polymer dynamics in an elongational flow. *Science* **276**, 2016–2021.

Stone, H. A., Nadim A. & Strogatz S. H. 1991 Chaotic streamlines inside drops immersed in steady Stokes flows. *J. Fluid Mech.* **232**, 629–646.

Sulik, K., Dehart, D. B., Iangaki, T., Carson, J. L, Vrablic, T., Gesteland, K. & Schoenwolf, G. C. 1994 Morphogenesis of the murine node and notochordal plate. *Dev. Dyn.* **201**, 260–278.

Taylor, G. I. 1969 Motion of axisymmetric bodies in viscous fluids. In *Problems of Hydrodynamics and Continuum Mechanics* pp. 718–724. SIAM.

Wu, T. Y. 1978 Slender-body theory for low-Reynolds-number flows. In *Symposium on Applied Mathematics, dedicated to the late Prof. Dr. R. Timman* (ed. A. J. Hermans & M. W. C. Oosterweld) pp. 191–202. Delft University Press.